A Framework for the Fabrication of Nanostructures by the Use of Energetic Beams to Pattern Nanoclusters

by

Vikas Anant

B.E., Electrical Engineering (2001)
The Cooper Union for the Advancement of Science and Art

Submitted to the
Department of Electrical Engineering and Computer Science
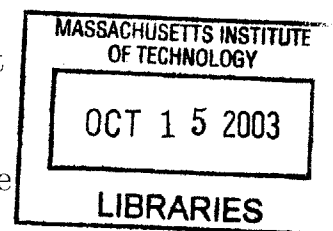in partial fulfillment of the requirements for the degree of

Master of Science in Electrical Engineering and Computer Science

at the

MASSACHUSETTS INSTITUTE OF TECHNOLOGY

September 2003

Author . . . .
Department of Electrical Engineering and Computer Science
August 29, 2003

Certified by. . . .
. . . .
Joseph Jacobson
Associate Professor of Media Arts and Sciences
Thesis Supervisor

Accepted by . . . . . .
. . . .
Arthur C. Smith
Professor of Electrical Engineering
Chairman, Department Committee on Graduate Students

A Framework for the Fabrication of Nanostructures by the Use of Energetic Beams to Pattern Nanoclusters

by

Vikas Anant

Abstract

Photolithography is fast approaching the optical limit for the minimum achievable structural dimension. A novel direct-write, hybrid top-down patterned/bottom-up fabrication approach, termed *nanoxerography* is proposed which circumvents the problem by using nanoclusters as the building blocks for nanostructures, and ion and electron beams to pattern the nanoclusters and build the desired structure. This thesis tackles two problems, one experimental and one theoretical, facing the realization of this process. Experimentally, charge patterns implanted with electron and ion beams are detected via kelvin force microscopy (KFM). Theoretically, simulation work is presented that addresses the accuracy of positioning clusters that arrive with high velocities onto predefined charge patterns on a substrate.

Thesis Supervisor: Joseph Jacobson
Title: Associate Professor of Media Arts and Sciences

Acknowledgments

This thesis is dedicated to my parents and my brother, who have got me this far and made me who I am.

I am grateful to Prof. Jacobson for the opportunity to pursue this research, and the inspiration and motivation to make it fruitful.

I would like to acknowledge my labmates (Vikrant Agnihotri, Brian Chow, Saul Griffith, William DelHagen, David Kong, David Mosley, Kie-Moon Sung, and Eric Wilhelm) for useful discussions, guidance, and making the lab a fun place, and Michael Houlihan for adminstrative support. I also acknowledge Jonathan Varsanik for his great work in helping me scout the best substrate for doing experimental KFM work.

I thank my many friends at MIT for enlivening my experience.

Contents

List of Figures

9

List of Tables

Chapter 1

Introduction

1.1 The Problem

Integrated circuits are manufactured today using highly sophisticated tools and processes to the most stringent specifications, which require engineering precision and uniformity of structures on the order of tens of nanometers or less. An evolution to smaller structures heavily depends on advances in photolithography, where light is used to expose a predefined pattern on a substrate coated with a resist. This top-down based method is approaching an engineering limit. Lasers, lenses, defect-free masks and high sensitivity resists are becoming increasingly difficult to engineer to the required specifications. For example, pattern transfer necessitates lens roughness to be on the order of angstroms, which has been one factor in the inability of the industry to keep up with the forecasts of the ITRS roadmap [1]. The cost in trying to achieve these specifications has also increased. Mask and lens costs now dictate a large portion of any integrated circuit development, in addition to the monetary costs on the order of hundreds of millions of dollars associated with setting up a fabrication facility. A solution to this problem is sought: one that reduces cost while increasing device density, complexity and reliability.

13

1.2 The Proposed Solution

A hybrid top-down patterned/bottom-up fabrication approach, termed *nanoxerography* [2] is proposed which uses nanoclusters as a building block in order to create the structures that define transistors, interconnects, and quantum-effect devices. In this process, a beam of clusters is formed using an apparatus that employs a sputtering process [3]. Collimation, charge and mass separation are performed to ensure uniformity of initial trajectory, velocity, size, and charge. An electrostatic pattern is formed on a substrate that has good charge retention properties using scanning electron and ion beams with resolution down to a few nanometers. Electrostatic forces direct the charged nanoclusters to the desired position. If sintering is desired, the clusters are then sintered using energetic beams: either laser, ion or electron beams, or via a hot-plate. Otherwise, the positioned clusters can serve as catalysts in chemical vapor deposition (CVD) growth, such as in the case of nanowires [4–7] and nanotubes [8–10] used to make functional devices [11, 12] and other interesting structures [13]. This process is termed *nanoxerography* because it is similar to xerography (see Figure 1-1), yet offers a vast difference in the scale of reproduction.
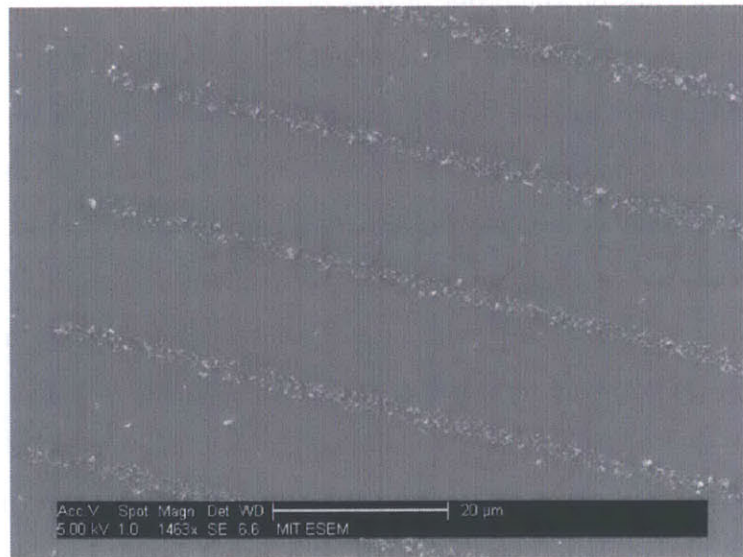
Figure 1-1: Electron micrograph of toner particles attracted to a pattern charged via an electron beam on spin-on polyimide. (courtesy of Jonathan Varsanik)

14

There are many advantages of the nanoxerographic process. The devices that can be manufactured can be three-dimensional, while the conventional approach dictates a two-dimensional planar device[1]. The nanoxerography approach employs an apparatus that is identical for different species of clusters - one only needs to tune certain controllable parameters. The entire process takes place under vacuum, thereby eliminating airborne contaminants. Visual feedback via electron beam imaging and elemental analysis is possible, making in-situ error correction possible. Changes in the charge pattern (hence structure of a device) are very easy to implement, as it only requires a change in software parameters, compared to the extensive turnaround time for mask manufacture or repair as in the case of optical lithography. The cost, both monetary and environmental, is also quite minimal, as it is primarily an additive process and does not require billion dollar fabrication facilities. However, possible disadvantages such as stitching accuracy of large patterns and throughput may require further engineering, although some of these are beginning to be tackled [16, 17].

1.3 Work Presented in this thesis

The work presented in this thesis presents a framework on which the proposed solution to the integrated circuit fabrication problem can be further developed and realized.

KFM Analysis of Charge Patterns

Chapter 2 tackles the problem of experimentally detecting surface charge implanted via electron and ion beams. Knowledge of the presence, magnitude and sign of charge is very important, and constitutes a cornerstone of the nanoxerographic process. In this thesis, measurements made via scanning kelvin probe microscopy (KFM), a form of electrostatic force microscopy (EFM) are presented, primarily for a spin-on polyimide electret.

---

[1]Some have used unconventional approaches to fabricate in three-dimensions, but with very little generality [14, 15].

Cluster Flight Simulation

Chapter 3 presents results of a simulation that addresses whether a given charge pattern can successfully attract clusters to itself, given some uncertainty in position and momentum. The parameter space of a test problem, given certain initial conditions, is explored. Additionally, analytical calculations are performed to calculate the trajectory of a particle in a simple case, and the veracity of the code is confirmed.

Chapter 2

KFM Analysis of Charge Patterns

One of the cornerstones of *nanoxerography* is the substrate on which a charge pattern is defined. One needs to understand the lateral charge resolution, charge retention and substrate alterations due to charging for a given substrate to be able to manufacture devices with minimal error. Kelvin force micrsocopy (KFM) provides for a method to measure, analyze and understand charge storage properties for a substrate. It can also enable a better understanding of the charging process and may be useful in analyzing electronic structures manufactured by nanoxerography in the future.

The use of an atomic force microscopy (AFM) to detect surface potentials evolved from using an AFM to do magnetic imaging [18]. While there exist many methods of detecting surface charge, scanning kelvin probe microscopy (KFM), a form of electrostatic force microscopy (EFM) was chosen because it was the method that offers the best lateral resolution for potential[1] maps. Many techniques have been developed that use the basic principles of KFM [20–22]. The method employed here was developed recently by Jacobs et al. [19, 23], theory for which is presented in Section 2.1.

---

[1] A very important point to note is that the potential that is measured via kelvin probe microscopy (KFM) is not the actual surface potential. Instead, the measured potential is a convolution of the actual surface potential with a transfer function [19].

(a) Neutral tip and sample before electrical connection

(b) Interaction force and electrostatic potential after electron diffusion

(c) External potential applied to zero the force
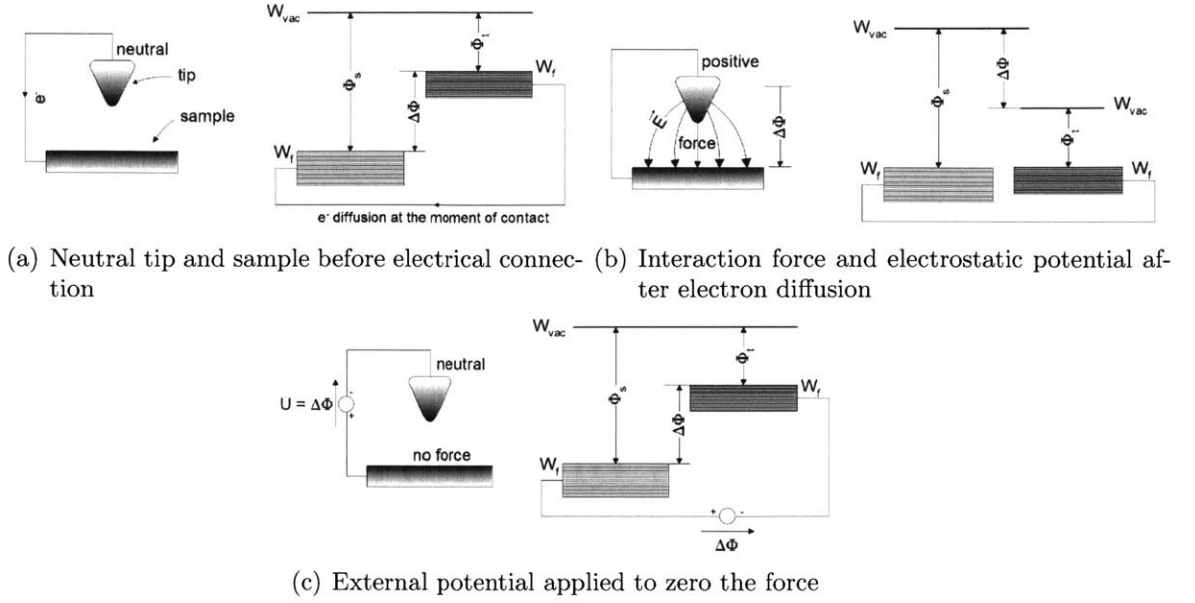
Figure 2-1: Energy diagrams of sample and tip (from [23], modified).

2.1 Theory

2.1.1 Contrast Mechanism for KFM

Contrast in KFM results from a difference in electronic work function[2] between the tip and the sample. Three scenarios that arise in KFM are depicted in Figure 2-1. We first consider the case when no potential is applied between the tip and sample.

As the energy diagram in Figure 2-1(a) shows, there is a disparity between the work functions of two materials. The tip has work function, Φ_t, while the sample, has work function Φ_s, measured from a common reference point, W_{vac}, the vacuum energy level. In this case, the tip has a smaller work function than the sample, therefore it is easier to remove electrons from it. When the materials come in contact, electrons will diffuse from tip to the sample. This is analogous to electron flow due to diffusion in a p-n junction, where two disparate materials are brought into contact (one that has a high concentration of electrons and the other that is depleted of electrons, or equivalently, is doped with "holes").

---

[2]The electronic work function of a material is the energy required to completely remove an electron from the surface.

When the diffusion process reaches equilibrium, as shown in Figure 2-1(b), an electrostatic potential difference forms between the sample and the tip, inhibiting further electron transfer. Another way to view this is that the fermi levels[3] equalize. In the case of a p-n junction, the flow of carriers eventually forms a depletion region due to the internal electric field, which inhibits the flow of more carriers. To enable carriers to flow in the p-n junction, a potential, known as the threshold voltage, that overcomes this internal electric field needs to be applied. In the case illustrated in Figure 2-1(b), the electrostatic potential difference that inhibits further diffusion of electrons between the tip and sample is given as $\Delta\Phi$. The electrostatic potential gives rise to a force between the tip and sample, which is also dependent on the first derivative of the capacitance between the two materials and will be discussed in Section 2.1.3.

In Figure 2-1(c), an external potential is applied that compensates the force between the tip and the sample. This external potential is equal to the difference of the work functions of the tip and the sample. For very large surface potentials, it may be possible to measure this external potential directly, but the force on the cantilever is usually weak. In scanning KFM, this potential, along with an sinusoidal (AC) signal is used in a feedback loop to measure the surface potential. The details are discussed in Section 2.1.3.

We now discuss how the work function relates to the surface charge for insulators such as those used in the experiments conducted for this thesis.

2.1.2 Work function for insulators

For an insulator, electrons are locked into the atomic structure, or in solid-state physics terminology, they fully occupy an energy band that is well below the Fermi energy. In order to charge an insulator, electrons must be "trapped" in localized higher energy states that exist due to impurities and defects. For a polymer, like polyimide or poly(methylmethacrylate) (PMMA), there are many defects arising from the amorphous nature of the material which can serve as traps where electrons with

---

[3]The fermi level is defined as the highest occupied energy level at 0 K.

sufficiently low energy can be trapped. An insulator with trapped electrons will have a lower work function than an insulator without any trapped electrons, as the energy required to remove the trapped electrons is much smaller than the energy required to remove electrons that reside in the atomic structure of the insulator. Due to the disparity in the work function, one can resolve a contrast difference in the KFM technique, similar to the manner described in Section 2.1.1.

We now discuss how the KFM potential is detected, and how surface charge is differentiated.

2.1.3 Force and KFM potential

The force that is felt on the tip due to the difference in work functions comes from a simple equation describing the stored electrostatic energy, U_{pp} in a parallel plate capacitor:

$$U_{pp} = \frac{1}{2}C(\Delta V)^2 \tag{2.1}$$

where C is the capacitance, ΔV is the potential between the plates of the capacitor, in this case, is given by

$$\Delta V = (\Delta\Phi - U_{DC})$$

where $\Delta\Phi$ is the potential between the sample and the tip due to difference in work functions, and U_{DC} is the external voltage applied on the tip. The force is the derivative of the electrostatic energy, U_{pp} with respect to z, the direction of free movement for the cantilever. The force, F_z is given by [23]:

$$F_z = \frac{1}{2}\frac{dC}{dz}(\Delta\Phi - U_{DC})^2 \tag{2.2}$$

Since the force is weak, feedback is employed by applying an AC voltage to the tip at frequency ω. Equation (2.2) becomes

$$F_z = \frac{1}{2}\frac{dC}{dz}(\Delta\Phi - U_{DC} - U_{AC}\sin\omega t)^2 \tag{2.3}$$

20

F_z in Equation (2.3) can be expanded to yield spectral components at DC, ω and 2ω [23]:

$$F_{DC} = \frac{1}{2}\frac{dC}{dz}\left((\Delta\Phi - U_{DC})^2 - \frac{U_{AC}^2}{2}\right) \qquad (2.4)$$

$$F_{\omega} = -\frac{dC}{dz}(\Delta\Phi - U_{DC})U_{AC} \qquad (2.5)$$

$$F_{2\omega} = -\frac{1}{4}\frac{dC}{dz}U_{AC}^2 \qquad (2.6)$$

The raw signal (collected by the split photodetector in the AFM) now has a component at ω, with a certain phase. The phase of this signal allows one to differentiate between positively and negatively charged regions on a sample. Where $\Delta\Phi$ is *positive*, the force will be *in phase* with V_{AC}, while a *negative* $\Delta\Phi$ will produce a force that is *out of phase* with V_{AC}. The ω component of the raw signal is multiplied by the sign of its phase and is inserted into the feedback loop which modifies the value of U_{DC} until the force, F_{ω} is zero. The ultimate value of U_{DC}, once feedback is complete, is the recorded potential for a given pixel. This process is repeated for every pixel in a scan area to form a potential map.

Figure 2-2 illustrates how the mechanical motion due to topography is decoupled from the motion due to electrostatics. In the first pass, the AFM is operated in tapping mode to collect topography data. In this pass, a mechanical oscillation is induced by applying an AC potential to the z-piezo near the resonance frequency of the cantilever, but no AC voltage is applied to the tip. Once the topography for a line trace is recorded, the oscillating AC potential on the z-piezo is removed, an AC voltage is applied to the tip, and the line is retraced at a constant height above sample. This mode of operation is termed "LiftMode™" by Veeco Instruments, manufacturers of the AFM used in the experiments, while the first pass is taken in "TappingMode™". Additionally, in order to maximize sensitivity, the applied AC voltage is chosen to have the same frequency as the resonant frequency of the cantilever in order to couple the force that results from a surface potential into mechanical motion.
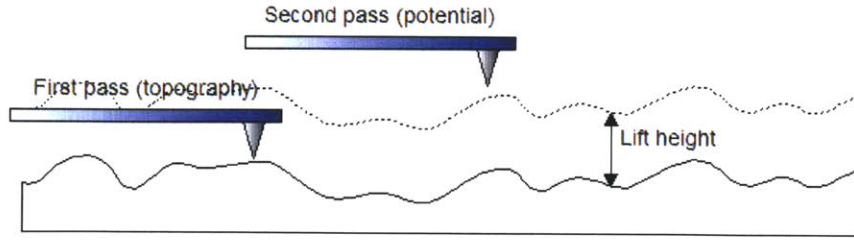
Figure 2-2: Kelvin probe method in lift mode
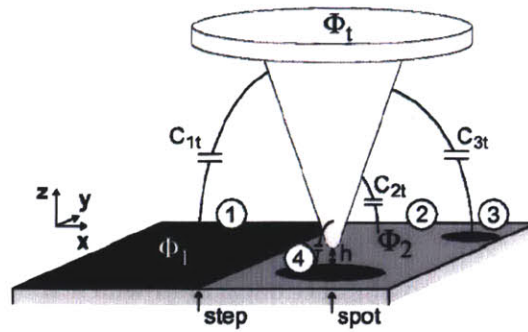
Figure 2-3: Sample-tip interaction (from [19])

2.1.4 Sample-tip interactions

In actuality, the measured potential is not only due to the capacitance between the sample region directly below the tip, but also due to nearby charged regions that can also contribute to mechanical motion of the cantilever, as illustrated in Figure 2-3. These contributions can be modelled [19] by expanding Equation (2.5) to include the contributions from all C_{it}'s, the capacitance between the tip and i^{th} region on the sample:

$$F_\omega = -\sum_{i=-1}^{n} \frac{dC_{it}}{dz}(\Delta\Phi - U_{DC})U_{AC}. \tag{2.7}$$

In effect, the measured potential is weighted by contributions from various surface regions, with distant regions contributing less than a region immediately below the tip. In addition, the potential Φ_1, of a large region, as shown in Figure 2-3, will appear smoothed out rather than abrupt, as it will start to contribute to the measured

22

potential even when the tip is a distance away from the step. Thus, the KFM potential will be a convolution of the actual potential distribution with some transfer function that depends on the geometry of the tip and the position of charged regions in relation to the tip on the sample. As Jacobs et al. point out, the KFM technique cannot yet map the actual surface potential distributions from measured values for structured surfaces that one cannot deconvolute easily. In addition, they also find that the cantilever surface dominates the local electrostatic interation when the tip diameter is too small, therefore they recommend the usage of a "long and slender but slightly blunted tip suppported by a cantilever of minimal width and surface area" [19].

2.2 Experimental Method

2.2.1 KFM

All KFM measurements were made on a commercial AFM (D3000, with Nanoscope®IIIa controller and Extender™Electronics Module, vendor: Digital Instruments, a division of Veeco Instruments) using the provided software (NanoScope®, version 4.42r4). These steps were sequentially followed:

1. The extender module is set to surface potential.

2. The cantilever is loaded, and the laser is aligned to the tip end of the cantilever.

3. The resonant frequency of the tip is found. At this point, the software also reads out the drive amplitude (the potential applied to the z-piezo to induce cantilever oscillations). If the drive amplitude is too high (for the OSCM-PT tips used, the acceptable range was between 350mV to 650mV), then the tip is removed, reseated and the procedure is repeated.

4. The resonant frequency is noted, and shifted approximately 0.1 kHz off-peak for imaging in tapping mode.

5. A good tapping mode image is obtained.

6. The feedback parameters in *interleave* mode are now set. The `drive frequency` and `drive phase` for the second pass scan are set in this panel. The `drive frequency` is set to the frequency of the resonant peak, while the `drive phase` is set to $-90°$. In addition, the `input feedback` variable is set to `potential`. The main parameters one has to optimize in order to get a good potential image are:

   (a) `lift scan height`: height above the topography that the potential scan is taken,

   (b) `fmigain` and `fmpgain`: the integral and proportional gain, respectively, for the feedback loop used in the second pass,

   (c) `drive amplitude`[4]: AC bias applied to the tip.

Generally, slow scans (1 scanline/second) with a large number of pixels per line (256 or 512) were taken.

The characteristics for the tips used in the images presented in this thesis are given in Table 2.1, while electron micrographs of the NSC15 and OSCM-PT tips are given in Figures 2-4(a) and 2-4(b). (Source: `http://www.spmtips.com/cantilever/2.0.0.33` for NSC15 tip, `http://store.veeco.com` for others). Specifically, the NSC15 tip was used to collect the image shown in Figure 2-11(a), MESP tip was used to collect the topographical image in Figure 2-8, while the OSCM-PT tip was used for all surface potential images.

2.2.2 Sample Charging

To charge the substrates, a commercial environmental scanning electron microscope was used (FEI XL30 ESEM with a Field Emission Gun (FEG) with NPGS, Nanometer Pattern Generation System, to enable patterning, Manufacturer: FEI Company for ESEM, JC Nabity Lithography Systems for NPGS). Ion beam charging was performed with a focussed ion beam (microscope) (FEI DB235 with custom written software

---

[4]This drive amplitude is in the *interleave* panel, and is different from the one in step 3.

Table 2.1: Typical/range of values for various tips used for imaging

Parameter	NSC15 (tapping only)	MESP (tapping,potential)	OSCM-PT (tapping,potential)
Type	Si with Al coating on backside	Si with magnetic film, Au coating on backside	Si with PtIr coating
Cantilever Length	125μm	225μm	240μm
Cantilever Width	35μm		
Cantilever Thickness	4μm		
Resonance Frequency	325kHz	60-100kHz	70kHz
Force Constant	40 N/m	1-5 N/m	2 N/m
Tip cone at apex	20° - 25°		
Tip half angle		17° side, 25° front, 10° back	
Tip height	15-20μm		14μm
Typical tip curvature	<10.0nm	25-50nm	
Vendor	MikroMasch	Veeco Instruments	Veeco Instruments

to enable patterning, Manufacturer: FEI Company). The uncharged samples were prepared less than 24 hours before the charging process in most cases, in other cases, were kept in a nitrogen environment. Imaging was commenced on charged samples within 10 minutes of removing from vacuum.

2.2.3 Imaging a Standard Sample

In order to interpret the images produced by the KFM method, various parameters were altered while imaging a "standard" sample. The standard sample consists of two isolated metal pads with interdigitated lines that are 10μm wide with a 10μm pitch.

In the first test, the surface potential was varied, while the lift height and AC bias applied to the tip were held constant. The results are shown in Figure 2-5, while the imaging conditions are given in Table 2.2. The ground and "earth" electrodes of the power supply were connected to the ground pin in the instrument, which is also connected to the stage. Figure 2-5(a) shows the conditions applied for each segment of the image. Figure 2-5(b) shows a three dimensional profile of the surface potential

(a) NSC15 Tip   (b) OSCM-PT Tip
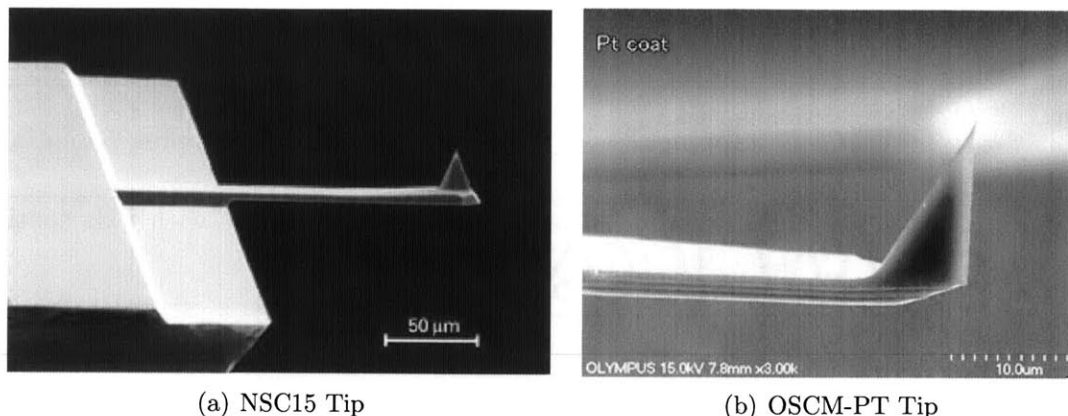
Figure 2-4: Electron micrographs of various tips used for imaging

Table 2.2: Imaging conditions for Figure 2-5

tip AC bias, U_{AC}	1000 mV
lift height	5 nm
surface potential	varied

map while Figure 2-5(c) shows profiles of two scan lines of the surface potential map.

It is interesting to note that while one may expect the ground electrode to be at the same potential throughout the image, it does not stay at that potential. One possible explanation is that we detect image charge induced by surface charge present on the left electrode, whose sign is *also* inverted when the sign of the potential on the left electrode is inverted, say from 1V to -1V.

As expected, the horizontal profile in Figure 2-5(c) is smoothed out as the tip traverses from one electrode to the other. Although it is difficult to discern from the vertical profile in Figure 2-5(c) because the contrast is adjusted to accommodate the higher potentials, the steps in Figure 2-5(b) show that it is possible to detect potentials as low as 10mV. Jacobs et al. report that their equipment[5] can detect potentials as low as 4mV with potential noise less than 1mV [23], while the DI3000 manual quotes a noise level of 10mV. Another point to note is that the surface potential data does not correspond to the actual potential on the electrodes, as it is a function of height (capacitance) and other geometric factors (tip size and shape), difference in

---

[5]They have a MultiMode™AFM while a DI3000 AFM is used in this case, and deposit a 6nm Pt-C film on the tip instead of Pt-Ir.
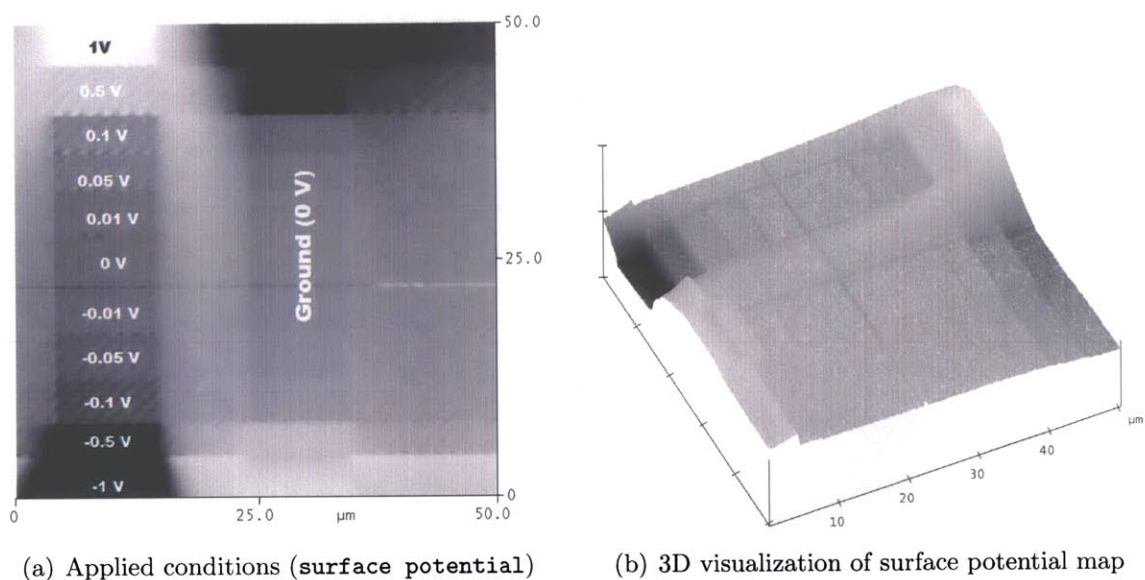
(a) Applied conditions (`surface potential`)

(b) 3D visualization of surface potential map
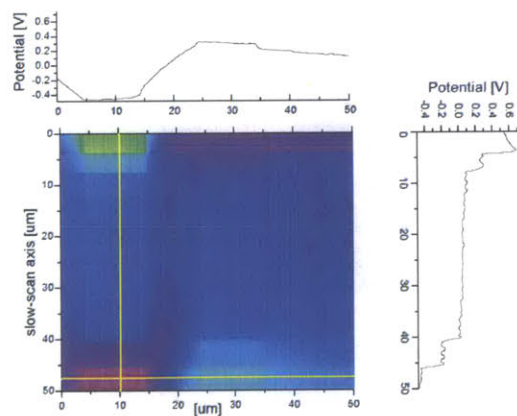
(c) Profiles of two scan lines of surface potential

Figure 2-5: Surface potential data of standard sample where surface potential was varied

work function due to the material of the tip and sample, and electrostatic surface potentials.

Another test was conducted where the lift height and AC bias applied to the tip were varied, while the potential applied to the electrodes was held constant. The results are shown in Figure 2-6, while the imaging conditions are given in Table 2.3.

Figure 2-6(a) shows that at a 0V AC bias, there is no topography detected, though Figure 2-6(b)(i) shows that the detected voltage increased as the tip was scanned from one side to the other. This occurs at all lift heights, therefore suggests that this is

Table 2.3: Imaging conditions for Figure 2-6

tip AC bias, U_{AC}	varied
lift height	varied
surface potential	+500 mV on left electrode with respect to right electrode

(a) Applied conditions (`AC tip bias, lift height`)

(b) Plots of horizontal cross-sections at AC tip bias equal to (i) 0mV, (ii) 100mV, (iii) 500mV and (iv) 1000mV for various lift heights
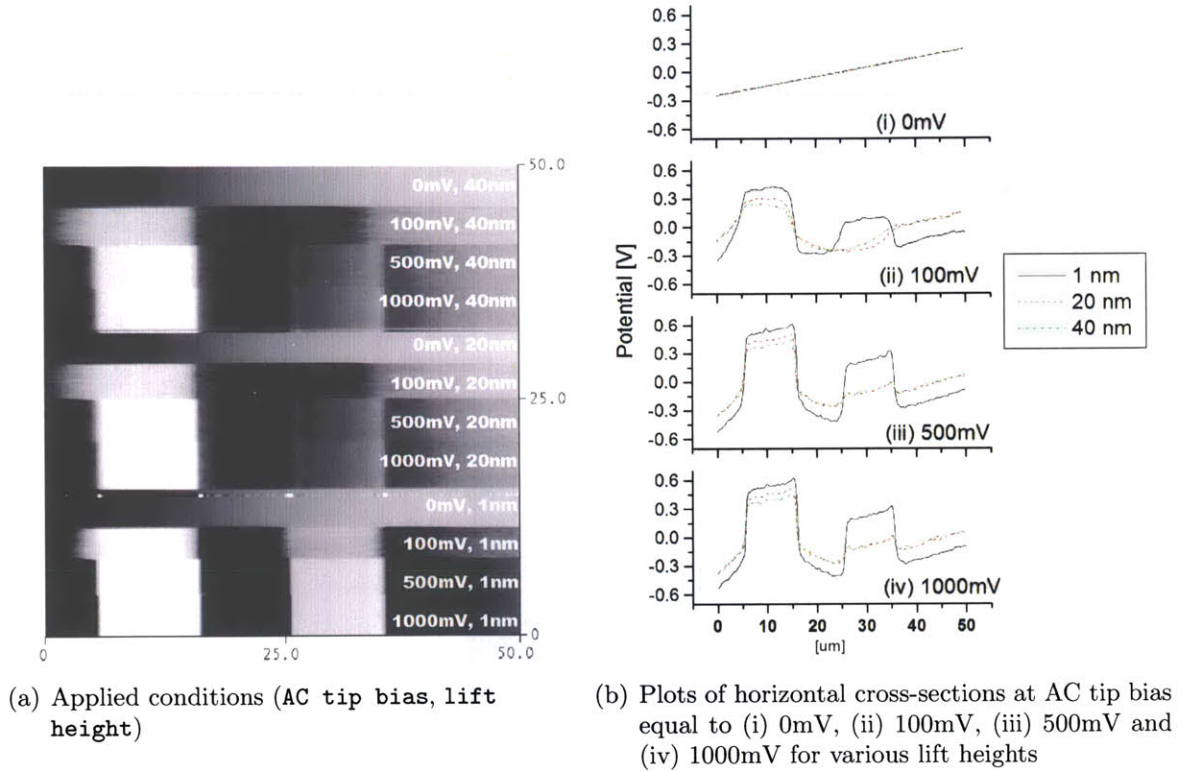
Figure 2-6: Surface potential data of standard sample where lift height and AC tip bias were varied

a background that is independent of lift height and can be removed from the other plots. Thus one can assume that the slanting plateau (from 5μm to 15μm) on each of the line plots in Figures 2-6(b)(ii), (iii) and (iv) can be modified to a flat plateau if this background is subtracted. The reason for the sloped background reading is not known, but may be due to piezo drift.

Another striking feature of Figure 2-6(b) is that scans with 1nm lift height tended to map topography much more than the 20nm or 40nm scan for all AC biases, but there is very little difference in the 20nm and 40nm lift height scans. An increase in the AC bias tends to amplify the signal slightly, in addition to producing straighter

28

sidewalls, as can be seen in the sharper sidewalls in Figure 2-6(b)(ii) compared to 2-6(b)(iii).

2.3   Sample Preparation

The ideal sample for the experiments is one that

1. charges well, preferably retains charge for extended periods of time to allow for image collection time;

2. does not get damaged by the method of charging, which in this case, is an electron beam with acceleration voltages in the range of a few kiloVolts (kV) up to 30 kV;

3. is very flat, to avoid surface topography in interfering with the surface potential map;

4. has a registration process that is

   (a) visible in the scanning electron microscope (SEM) so that large portions of the sample need not be charged;

   (b) visible optically, as a visual guide for determining where to approach the sample with the AFM tip;

   (c) does not affect the flatness and other properties of the sample.

It was found to be very difficult to fulfill these requirements entirely. Some results are given in Section 2.3.1 for a PMMA-coated silicon substrate that passed many of these requirements, but retained too much damage upon charging. Another substrate that was tested extensively was aluminized Polyethylene Terepthalate (mylar) film, which proved to be difficult to image because of large topographical features and possibly too much tip/cantilever-sample interaction. The substrate that was finally chosen for the many experiments was spin-on polyimide, results for which are described in Section 2.4.

2.3.1 PMMA

The literature has many results pertaining to charging PMMA using an electron beam [24-27]. Another compelling reason to experiment with this polymer was that imaging of PMMA via KFM has been performed [28], where charging was performed via contact with a metalized stamp held at a potential. Therefore, there was interest in trying to image stored charge in PMMA via KFM, but where the charge is injected via an electron beam.

The sample was prepared in the following manner:

1. A Si wafer (n-type, 1-5 Ω/cm^2, [100], polished) was plasma-cleaned (5min, 50sccm O_2 at 50W, 1 Torr).

2. A thin film of PMMA (PMMA 950K Microchem 3% in chlorobenzene) was spin-coated (6000rpm for 30s).

3. The sample was baked to ensure complete solvent evaporation (1 hour, 90C in N_2 atmosphere). The thickness of the sample was measured by ellipsometry and was found to have a mean of 208.0nm with a standard deviation of 1.1nm over the substrate (10 sample points). The local RMS roughness was found to be 0.250nm (found via AFM analysis).

4. An electron beam checkerboard pattern was written in several positions using the ESEM and NPGS (accelerating voltage: 30kV, beam current: 170 $\mu C/cm^2$). This checkerboard is to be used as a registration mark that can be seen optically and in the SEM. The width of each square is 10μm, which is an ideal scan size for the AFM. The width of the entire checkerboard pattern was 100μm.

5. The sample was developed in PMMA developer for 30 seconds (see Figure 2-7(a)).

6. A 200μm charge pattern composed of 1μm diameter circles with 2μm center-to-center spacing was exposed at 2.5kV and various doses ($150\mu C/cm^2$, $100\mu C/cm^2$,

30
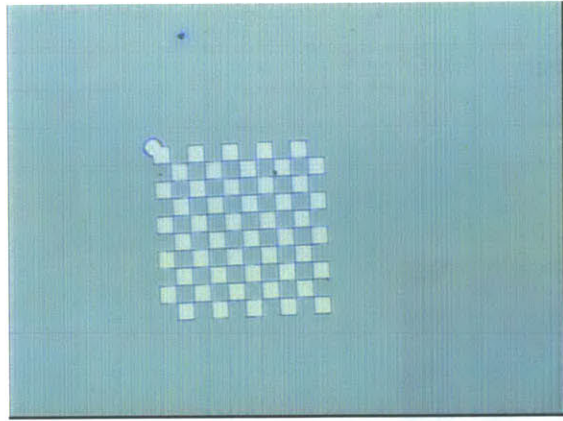
(a) Optical image of PMMA with developed checkerboard pattern
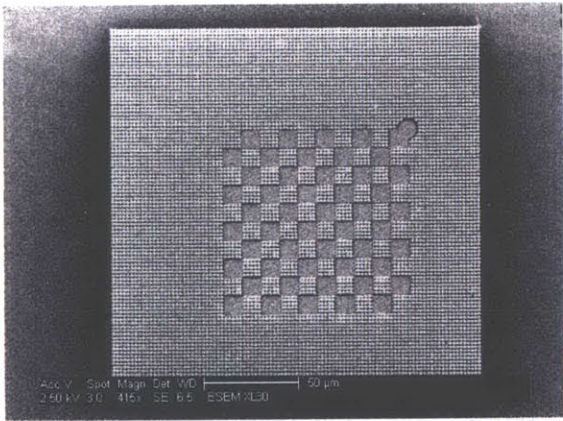
(b) Electron micrograph of checkerboard (after development) with larger charge pattern of circles
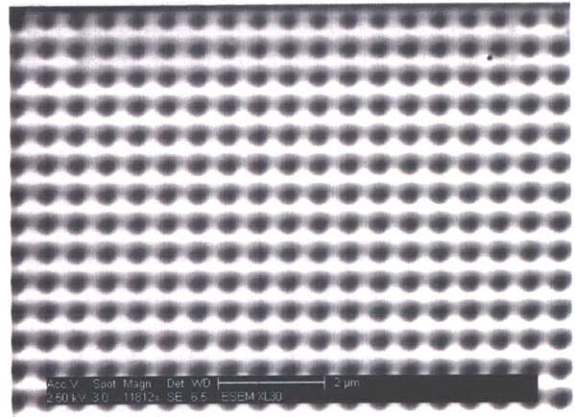
(c) Electron micrograph (voltage contrast image) of $1\mu m$ charged circles

Figure 2-7: PMMA sample preparation

$50\mu C/cm^2$, $30\mu C/cm^2$, see Figure 2-7(c)) over an area that included the $100\mu m$ checkerboard pattern (see Figure 2-7(b)).

After charging, the sample was imaged in the AFM in tapping mode using an MESP tip (see Table 2.1) to look for damage due to electron beam radiation. Figure 2-8 clearly shows the extent of the damage. The particular conditions that were used are given in Table 2.4. Note that the quantity for deposited charge density in this table is a *desired* quantity as opposed to the actual surface charge. Some of the charge will leak via the substrate or as backscattered electrons. Figure 2-8(b) shows there is a prominent raised lip with a height of 22nm above the zero height, while there is an 11nm deep depression where the circle is located.

Table 2.4: Sample and imaging conditions for Figure 2-8

Deposited charge density	$50\mu C/cm^2$
Accelerating voltage	2.5kV
Tip used	MESP

(a) Tapping mode image of PMMA surface after charging

(b) Cross-section at AA'
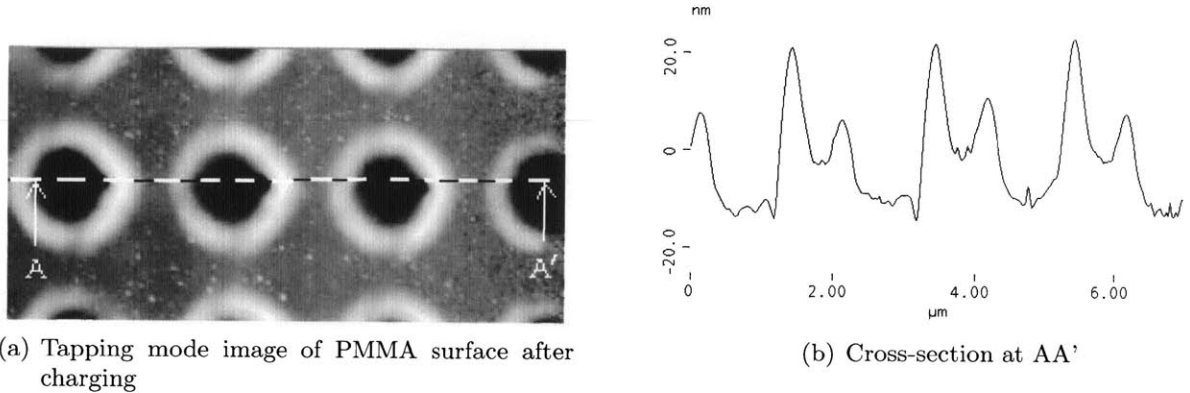
Figure 2-8: Electron beam-induced damage in PMMA.

As a result of the clear damage visible at a relatively low accelerating voltage, further experiments on PMMA were abandoned and other substrates that had more resistance to electron bombardment were sought. One substrate that demonstrated more resistance was polyimide, but the surface was not as smooth as that of PMMA. The manner of substrate preparation was different for polyimide, as it does not possess the resist-like properties that were exploited for PMMA to make the checkerboard registration mark. This is further discussed in Section 2.3.2.

2.3.2 Spin-on Polyimide

For the two sets of experiments that produced positive KFM results, the registration mark on the sample was produced in different ways. A transmission electron microscopy (TEM) grid that had letter/number indexed squares was used in both cases. In one case, it was dropped onto the surface before the bake step, while in the other case, it was used as a mask for gold deposition via evaporation. The specifics of the TEM grid used are given in Table 2.5. The following subsection describes the first method of sample preparation.

Table 2.5: Parameters for TEM grid used in sample preparation

Vendor	Stucture Probe, Inc.
Name	Regular SuperGrid with Slim Bars
Bar width	30μm
Exposed grid dimension	95μm
Grid thickness	20μm
Formvar coating	not present
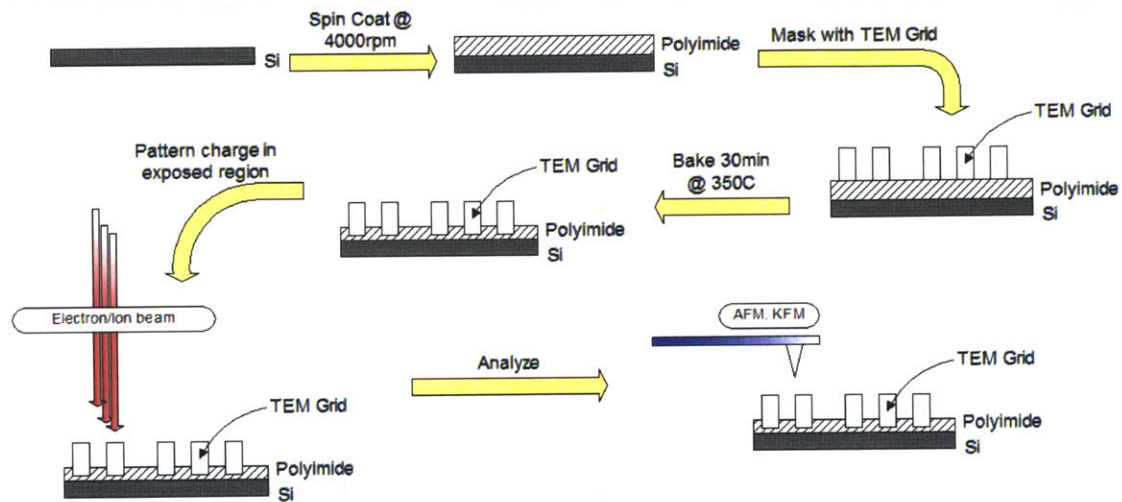
Figure 2-9: Sample preparation process where a sunken TEM grid is used as registration

Sunken TEM grid as registration

The sample was prepared in the following manner, also outlined in Figure 2-9:

1. Polyimide (PI2613, Pyralin® Polyimide Coating, vendor: HD MicroSystems™) was spin-coated (2mL spun at 4000rpm for 40s) on Si wafer (polished, 1-5Ω/cm^2, n-type, [100]). This should produce a thick coat of polyimide ($\sim$2.4μm).

2. TEM grids were placed on sections of the wafer, and the wafer was baked at 350°C for 30 minutes. In this process, the TEM grid sunk in the polyimide as the solvent was being removed.

3. The sample is then exposed in the ESEM with a given pattern, following which it is taken to the AFM to be analyzed.

33

This method was used to prepare samples for all sections except where the ion beam was used to charge the sample (Section 2.4.3). One disadvantage of this sample preparation method is that the edges of the exposed region in each square were distorted due to pinching. Though the imaging was done towards the center of the TEM grids, another registration method that does not impact the topography was sought. One solution that was tested was simply to attach the TEM grid via copper tape to the sample. This method was not able to produce any AFM images, possibly because the 20μm thickness of the grid does not allow for the tip to get into close proximity with the topographical features of the sample. Therefore, another method was employed to ensure only the registration technique had a very small thickness and did not interfere with the imaging process.

Evaporated gold through a TEM grid as registration

The sample was prepared in the following manner, also outlined in Figure 2-10:

1. Polyimide (PI2613, Pyralin® Polyimide Coating, vendor: HD MicroSystems™) was spin-coated (2mL spun at 4000rpm for 40s) on Si wafer (polished, 1-5Ω/cm^2, n-type, [100]). This should produce a thick coat of polyimide ($\sim$2.4μm).

2. The wafer was baked at 350°C for 30 minutes.

3. A TEM grid was taped using copper tape onto a chipped portion of the wafer, leaving the indexed part of the grid exposed.

4. Gold ($\sim$5nm) was evaporated thermally.

5. The grid was removed, and the sample is exposed in the FIB with a given pattern, following which it is taken to the AFM to be analyzed.

The added advantage of this technique is that a much smaller area (30μm as opposed to 95μm) can be found via following the letter/number indices. The disadvantage is that the gold evaporation was not clean, possibly due to surface migration or other causes, such that there was gold on the parts of the substrate that were nominally masked by the TEM grid.
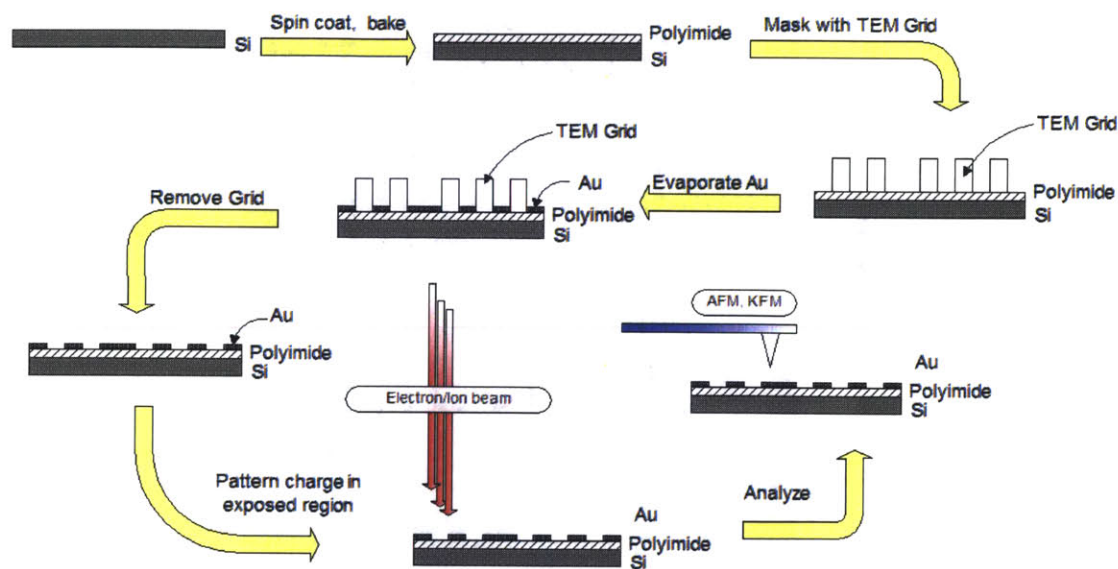
Figure 2-10: Sample preparation process where gold is evaporated using a TEM grid as a mask

2.4 Experimental Results for Spin-on Polyimide

2.4.1 Topography study

The topography of the spin-on polyimide sample was mapped. First, a tapping mode image was taken with an NSC15 tip, which is sharper than the OSCM-PT tip used for potential imaging. The images shown in Figure 2-11 show that the image taken with the OSCM-PT tip is blurrier than that taken with the NSC15, suggesting that the OSCM-PT tip has a tip apex that is not as sharp as the NSC15, which better suits the KFM technique [19].

The RMS roughness was found to be 5.100nm (4.804nm after a "flatten" operation was performed to compensate for global tilt of the substrate), which is much larger than that of PMMA. Though this is a rough substrate, the roughness is uniformly distributed over the substrate, so its effect on the potential maps may be better understood with an appropriate background reading.
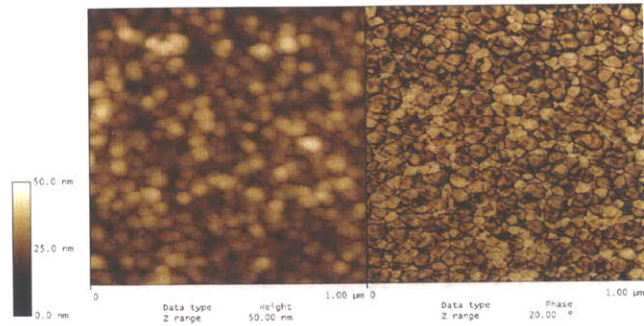
(a) NSC15 tip used
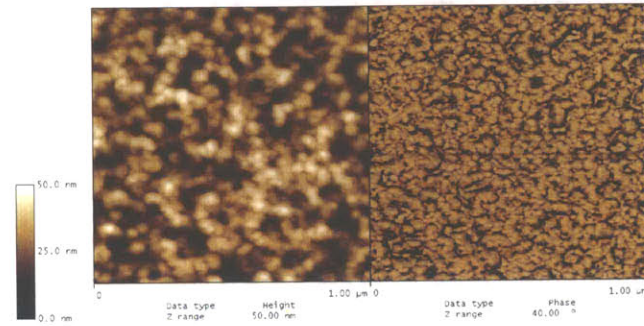
(b) OSCM-PT tip used

Figure 2-11: Topography and phase map (tapping mode) of spin-on polyimide samples

Table 2.6: Sample and imaging conditions for Figure 2-12

Deposited charge density	$8000\mu C/cm^2$
Accelerating voltage	2.5kV
Tip used	OSCM-PT
AC tip bias	7083mV
Lift height	1nm

2.4.2 Electron beam-induced charge patterns

Background potential map

A potential map within a square in the TEM grid that was not charged via the electron beam was taken to get a background reading of this sample. The data is shown in Figure 2-12, while the imaging conditions used are noted in Table 2.6.

As this null reading shows, there is a contribution to the reading from the background, but it is randomly distributed.
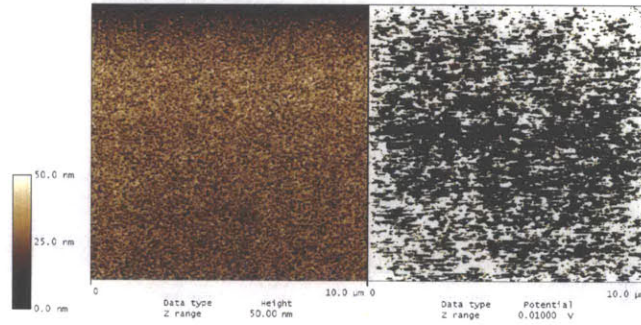
Figure 2-12: Topography (left) and potential (right) map of polyimide (background)

Table 2.7: Sample and imaging conditions for Figure 2-13

Figure	2-13(a)	2-13(b)
Deposited charge density	$8000\mu C/cm^2$	
Accelerating voltage	10kV	
Tip used	OSCM-PT	
AC tip bias	1000mV	7083mV
Lift height	10nm	1nm

Charging at High Dose

In order to chose an appropriate beam current, the large areas on a sample were subjected to varying doses, and then the sample was dipped in toner. It was found that a very clean transfer of positively charged toner occurred when $8000\mu C/cm^2$ of current was delivered to the substrate. Another sample prepared as illustrated in Figure 2-9 was charged with a pattern that had recurring $1\mu m$ squares with a $1\mu m$ edge-edge spacing in the horizontal direction and a $2\mu m$ spacing in the vertical direction with this beam current. The data is shown in Figure 2-13, while the imaging conditions used are noted in Table 2.7.

Repeat of study with another pattern (circles)

This experiment was repeated with another pattern, this time composed of $1\mu m$ circles spaced by $1\mu m$. The results are shown in Figure 2-14 and associated conditions are given in Table 2.8.

Figure 2-15 shows a cross-section that shows the peak-to-peak amplitude of the
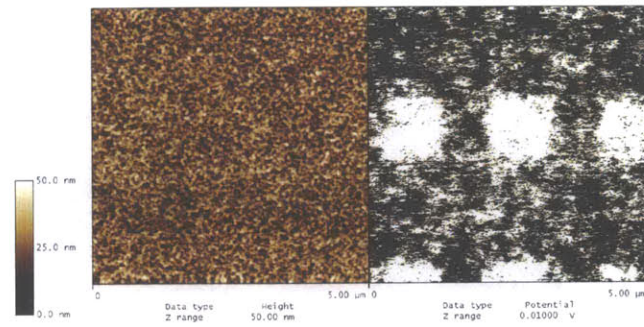
(a) Topography and surface potential map
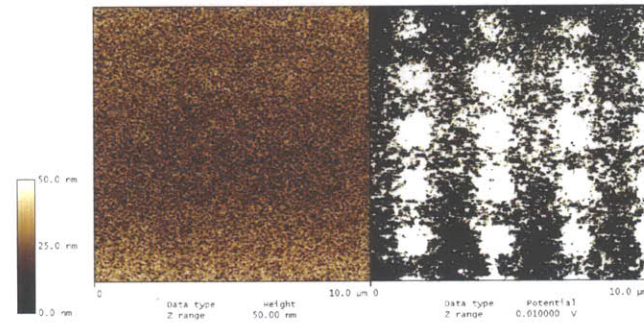
(b) Larger field of view, direction of scan is rotated 90° with respect to (a)

Figure 2-13: Potential map of charge pattern (1μm squares)

envelope for the potential map[6] to be 200mV. This figure also shows that, although this is a very high beam current, the topography of a charged section does not suggest damage, as there does not appear to be an underlying envelope for the topography cross-section (given in red, light grey if in b/w).

Charge retention study

The sample imaged in Figure 2-14 was left in ambient lab conditions for five days and then reimaged. The resulting image is shown in Figure 2-16, with imaging conditions shown in Table 2.9.

The sample appears to have experienced some discharge, as the once well defined circles appear disfigured. Charge decay can be attributed to discharge via ionization of water vapor from the air. As polyimide film is also known to absorb up to 1%

---

[6]The contrast in the potential maps in Figure 2-15 has been adjusted to ensure that the potential curve fits in the limits of the cross-section plot

Table 2.8: Sample and imaging conditions for Figure 2-14

Figure	2-14(a)	2-14(b)
Deposited charge density	$8000\mu C/cm^2$	
Accelerating voltage	10kV	
Tip used	OSCM-PT	
AC tip bias	1000mV	7083mV
Lift height	1nm	1nm
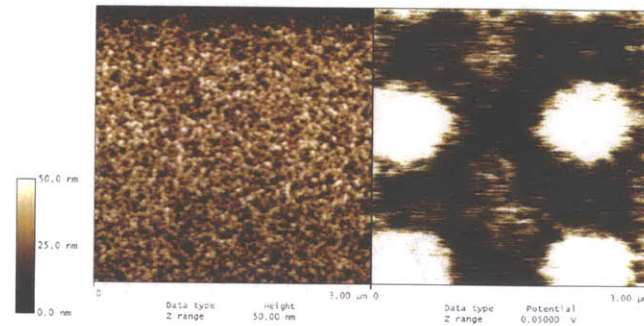
(a) Topography and surface potential map
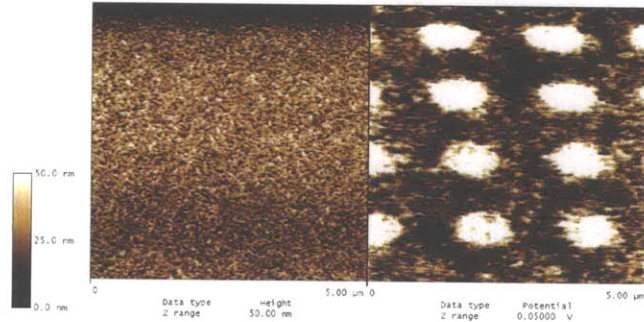
(b) Larger field of view

Figure 2-14: Potential map of charge pattern ($1\mu m$ circles)

water, it is also possible that the film may have swelled and disrupted the surface.

Charging at various dose levels

In order to repeat the preceding experiments for various dose levels, a few issues needed to be resolved. The first issue was that a very short charging time was desired, while being able to vary dosages. It was desirable not to expend too much time per pattern, otherwise there would be time for the charge to diffuse. Since the
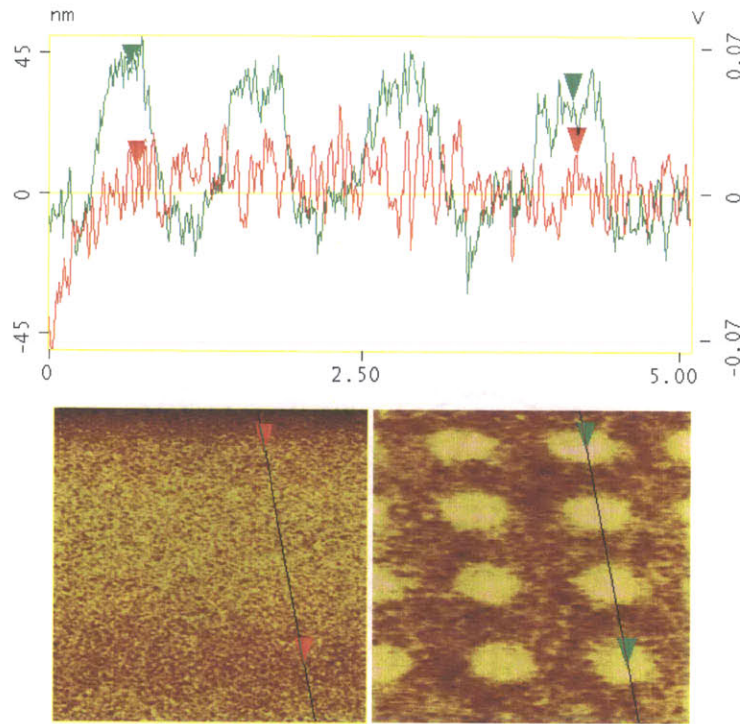
Figure 2-15: Cross-section of the potential map given in Figure 2-14(b)

Table 2.9: Sample and imaging conditions for Figures 2-16(a) and 2-16(b)

AC tip bias	1000mV
Lift height	1nm

focal point and dose are different for different spot sizes[7] in the ESEM, it is also not desirable to spend time refocussing the electron beam and measuring the dosage. Additionally, there is a limitation on the NPGS hardware, in that it is not able to dwell less than $10\mu s$ per scanned pixel. This meant that the lowest dose for a total beam current of ~500pA, if one wanted to expedite the writing of a pattern with a dose of $8000\mu C/cm^2$, was $700\mu C/cm^2$. A sample was charged with a few values in this range. The surface potential maps for various doses are shown in Figures 2-17 and 2-18 with imaging conditions shown in Table 2.10.

Figure 2-18 shows high frequency oscillations and several horizontal streaks across

---

[7]The spot size parameter electromagnetically controls the amount of current that is allowed to pass through the final lens. This controls the so-called spot size, since electron-electron repulsion dominates the widening of spot size at high electron flux densities. The dose is controlled by the **spot size** parameter in the ESEM controlling software and dwell time per pixel in the NPGS software.

(a) Topography and surface potential map

(b) Potential map of a 3μm scan area
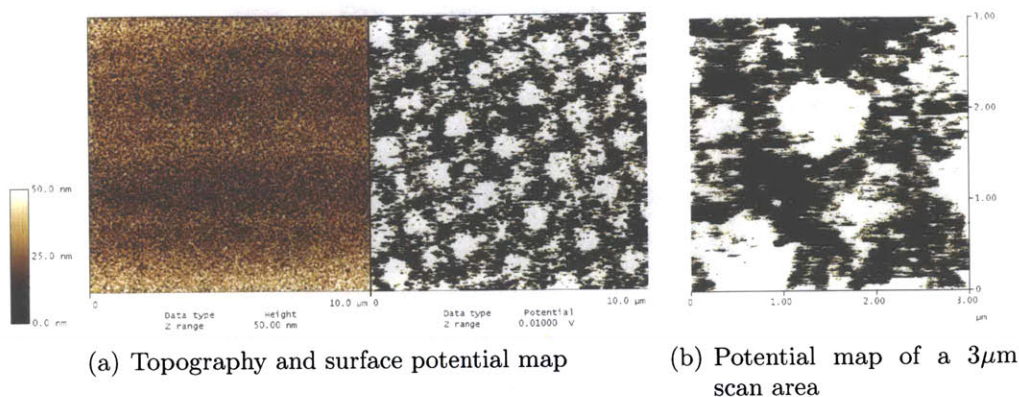
Figure 2-16: Potential map of charge pattern (1μm circles), taken 5 days after exposure to ambient conditions

Table 2.10: Sample and imaging conditions for Figures 2-17(a), 2-17(b) and 2-18

AC tip bias	1000mV
Lift height	1nm

the images. This can be caused by tip contamination, or incorrectly set gain parameters in the AFM software. As a result, the normally granular topography of the polyimide appears to have horizontal abberations. However, despite the sub-optimal topography map, a well resolved potential map was obtained.

An intriguing result was that of an apparent charge reversal when the dose was decreased from 8000μC/cm^2 to 1000μC/cm^2, as seen by the inversion in contrast. The charge reversal was still evident at a dose of 700μC/cm^2. This has been previously reported in theory [24] and experiment [29, 30] for PMMA. A plot from [24] is reproduced in Figure 2-19 that illustrates that reversal in sign. The mechanism proposed in [24] is that the positive potential is produced by "knock-on ionization of surface atoms under electron beam irradiation". A similar mechanism may be at play here.

2.4.3 Ion Beam Charge Patterns

An initial attempt at imaging ion beam charged patterns in spin-on polyimide was made with interesting results. A sample was prepared using the method illustrated
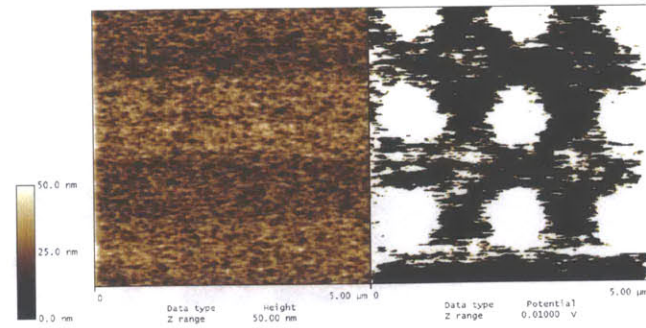
(a) Topography and surface potential, dose: $8000\mu C/cm^2$
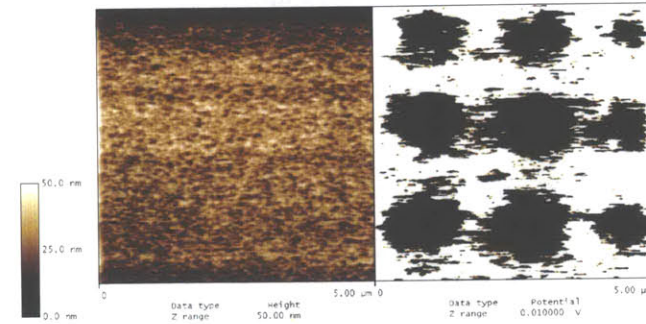
(b) Topography and surface potential, dose: $1000\mu C/cm^2$

Figure 2-17: Topography and potential maps of charge pattern where different charge doses were delivered to the sample

in Figure 2-10, where a thin layer of gold was evaporated through a TEM grid, and the sample was charged in the sections of the resulting pattern that did not have deposited gold. As there was gold that was scattered on the surface, a greater lift height was used in imaging to prevent contact with any gold that may have been dragged by the cantilever in the first pass.

A dose of $1000\mu C/cm^2$ was delivered to a sample at 30kV accelerating voltages for Ga^+ ions. The topography and surface potential map are shown in Figure 2-20, while the imaging conditions are given in Table 2.11. As one can see in the topography map, the level of detail seems to have diminished from earlier images, since the granular surface of the polyimide is not visible. This is not entirely understood but is thought to be due to tip/cantilever contamination, which may have resulted from the gold particles on the sample.

Figure 2-20 clearly shows extensive damage from the ion beam, evident from the dark squares in the topography image. The potential scan also shows dark squares,

(a) Topography and surface potential

(b) Larger area scan of surface potential
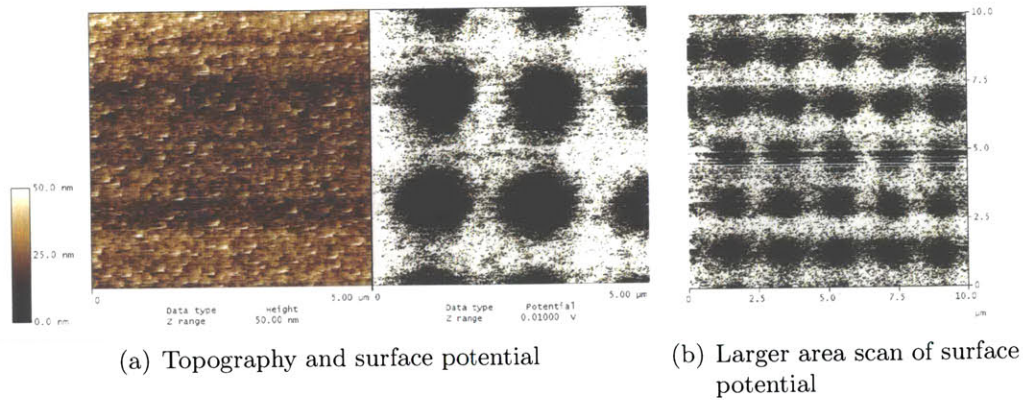
Figure 2-18: Topography and potential map of charge pattern (dose: $700\mu C/cm^2$)

Table 2.11: Sample and imaging conditions for Figures 2-20 and 2-21

Ion dose delivered	$1000\mu C/cm^2$	$33\mu C/cm^2$
Accelerating voltage	30kV	
AC tip bias	1000mV	2000mV
Lift height	50nm	50nm

which has opposite polarity as those encountered in the potential maps presented in preceding sections, which confirms the presence of positive charge in the sample. Also, there are dark shadows in the potential map that correspond to locations of gold on the topography, a result of different work function of the deposited gold than the polyimide, which in this case, is at a positive potential due to diffusion at the contact.

The experiment was repeated at a dose that was two orders of magnitude lower ($33\mu C/cm^2$). The hope was that the damage at this dose would be less. This was the case, as seen in the topography scan in Figure 2-21, conditions for which are given in Table 2.11. At this dose, however, a potential scan (even with a higher AC bias) did not result in any positive identification of surface charge due to ion implantation. Other features, such as the potential of gold evaporated particles (dark in image), were evident in the scan, suggesting that the scan was imaging the surface potential reliably.

43
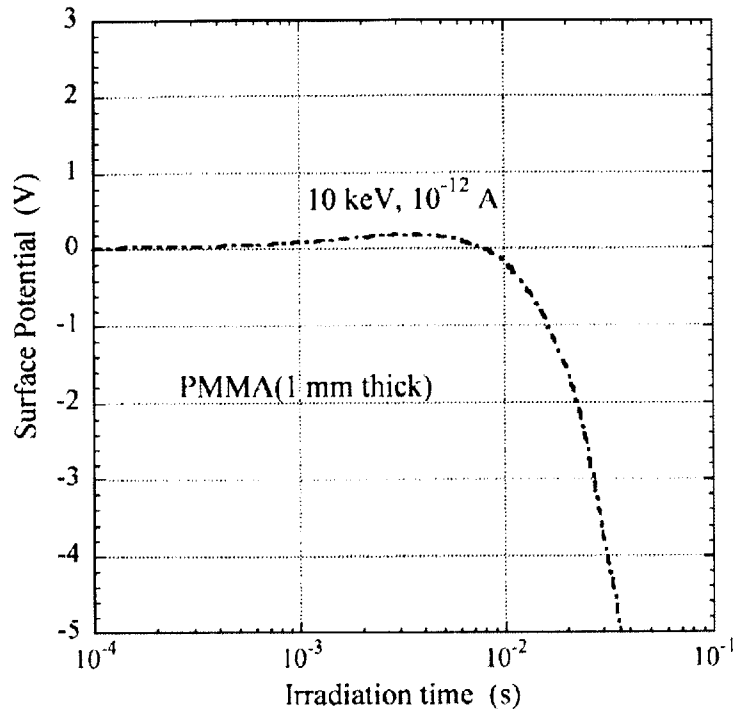
Figure 2-19: Time dependent surface potential (Theoretical result from [24])

2.5 Future work

Future work can be conducted in detecting surface potentials due to ion beam charging, as the literature is lacking in this regard. The effect of dosing can also be explored further for spin-on polyimide. Also, one would like to shift to the more traditional electrets, such as polyethylene terepthalate or polytetrafluoroethylene (PTFE), which tend to retain a greater quantity of charge. Most importantly, one would like to quantify and compare the readings, and get a true measure of the actual surface charge. This would require some theoretical calculations that take into account the tip-sample geometry, and tip/sample composition parameters to calculate the work functions.
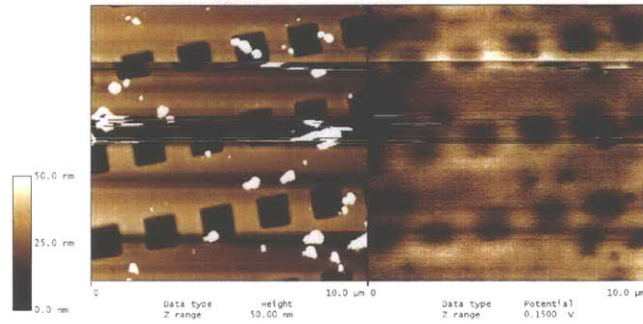
Figure 2-20: Topography and potential image of ion beam charged sample (dose: $1000\mu C/cm^2$)
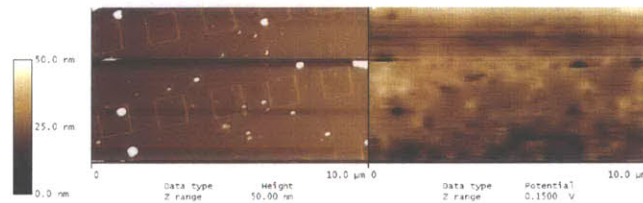
Figure 2-21: Topography and potential image of ion beam charged sample (dose: $33\mu C/cm^2$)

Chapter 3

Cluster Flight Simulation

One of the key concerns for the process of *nanoxerography* is the accuracy of positioning clusters that arrive with high velocities onto predefined charge patterns on a substrate. One method is to concentrate a large amount of charge at one point and hope that all clusters are diverted towards it. The problem with this approach is that there is a finite amount of charge that one can concentrate in a position, both due to surface confinement effects and electric breakdown, and it does not allow for rejecting clusters that are not fully aligned to hit their desired target. One approach is to surround an attractive potential by a repulsive one, creating an electrostatic "filter" that serves to reject clusters that are off-target, while only letting those through that have a certain trajectory, velocity, mass and charge. A simulation is presented in this chapter that tries to find the parameter space in which erroneous deposition can be minimized by using both positive and negative potentials, even if it is at the cost of rejecting clusters.

Section 3.1 presents the theoretical basis for this simulation. Krinke et al. [31] perform similar calculations but their system has many key differences, which are highlighted in this section.

47

3.1 Theory

Newton's second law describes the motion of a cluster towards a charged region on a substrate:

$$\vec{F} = m\vec{a} \tag{3.1}$$

where $\vec{F}$ is the force exerted on a particle with mass m to induce an acceleration $\vec{a}$. The force $\vec{F}$ can have many contributors, and is given by (3.2) [31]:

$$\vec{F} = \vec{F}_{drag} + \vec{F}_{stochastic} + \vec{F}_{external} \tag{3.2}$$

The first term, $\vec{F}_{drag}$ is given by [32]:

$$\vec{F}_{drag} = \frac{3\pi\eta_g d_p(\vec{v}_g - \vec{v}_p)}{C_c} \tag{3.3}$$

where η_g is the viscosity of the carrier gas, d_p the diameter of the particle, $\vec{v}_g$ the velocity of the carrier gas and $\vec{v}_p$ the velocity of the cluster and C_c a correction factor termed the Cunningham slip correction [32]. In our test case, we assume that 50 copper atoms compose the cluster, hence the diameter is an order of magnitude below 30 nm assumed by Krinke et al [31]. Moreover, since we assume the cluster is travelling ballistically in ultra high vacuum (UHV), viscosity plays a negligible role. Both these factors allow us to neglect the drag term.

The stochastic contribution to $\vec{F}$ in (3.2) plays a large part in Krinke's calculations when the particle is more than 100 nm above the substrate surface. Krinke et al give their particle velocity to be 0.3 ms^{-1} due to Brownian motion. In our test case, we assume that the particles have an average kinetic energy of 2.5 eV, which corresponds to 389 ms^{-1}, which is many orders of magnitude greater. The vast difference arises from the way in which clusters are generated in both cases. While Krinke et al produce clusters via thermal evaporation, we employ sputtering of a polycrystalline target. Coon and coworkers report copper clusters produced via sputtering by 3.75 - 3.9keV with Ar$^+$ to have a most probable energy in the range 1.6eV - 2.6eV [33]. We have assumed an average kinetic energy in the higher end of this range (2.5eV).

Hence we will be able to neglect the stochastic contribution to the force, but keep in mind that if the velocity drops to within an order of magnitude of 0.3 ms^{-1}, we will have to include this in the model.

The forces that contribute to $\vec{F}_{external}$ in (3.2) are given by [31]:

$$\vec{F}_{external} = \vec{F}_{lorentz} + \vec{F}_{image} + \vec{F}_{dipole} + \vec{F}_{vanderWaals} \qquad (3.4)$$

Of the forces that contribute to $\vec{F}_{external}$ in (3.2), the one that dominates far away from the surface is the Lorentz force, and is included. While the coulombic contribution to the Lorentz force is $\sim r^{-2}$, the other forces are generally inversely proportional to the fourth to fifth order in distance, hence are neglected in this simulation.

$\vec{F}_{lorentz}$ depends on the electric field $\vec{E}$, cluster charge q, cluster velocity $\vec{v}$, and magnetic field $\vec{B}$ and is given by the Lorentz equation:

$$\vec{F}_{coulomb} = q(\vec{E} + \vec{v} \times \vec{B}) \qquad (3.5)$$

In our case, we assume that the magnetic field $\vec{B}$ near the surface of the electret is negligible, although a magnetic field due current carrying coils in the vacuum chamber can contribute to this force.

The electric field is a function of the spatial coordinates, which in our simulations is assumed to be rectangular (in the verification example, spherical coordinates are used) and is considered time-invariant. In general, the electric field is not simple to derive analytically, so we use numerical methods to solve for it, as described in Section 3.2. After all the aforementioned simplifications and assumptions, the general equation that we must solve is:

$$m \begin{pmatrix} \frac{dv_x}{dt} \\ \frac{dv_y}{dt} \\ \frac{dv_z}{dt} \end{pmatrix} = q \begin{pmatrix} E_x(x,y,z) \\ E_y(x,y,z) \\ E_z(x,y,z) \end{pmatrix} \qquad (3.6)$$

Equation (3.6) is coupled because the velocity in the a given direction depends on
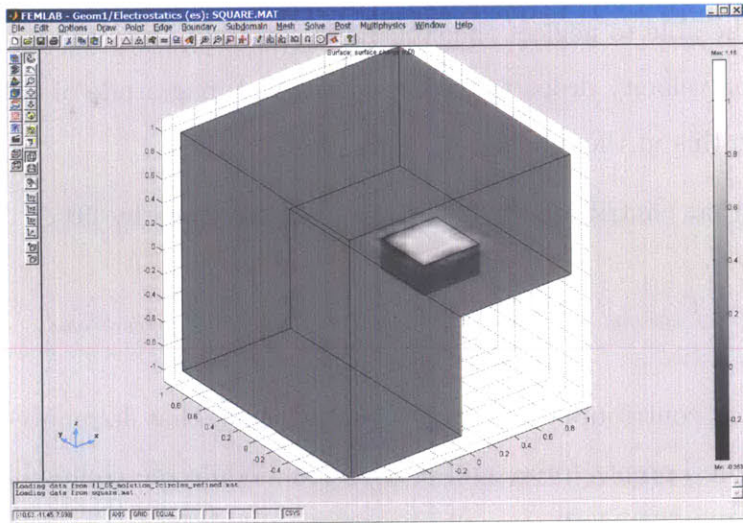
Figure 3-1: Surface charge density of a test geometry calculated and visualized in FEMLAB

the position in all space, so numerical methods are necessary to solve this equation at every time step. Euler's method and Runge-Kutta were used to solve this equation for the geometry and initial conditions presented in Section 3.4.

3.2 Software Design Flow

Code for the simulation was written in MATLAB and FEMLAB. FEMLAB is a package for MATLAB which allows for graphical input of geometry, boundary conditions and mesh conditions via a CAD-type interface, but can also be used via MATLAB-style functions. As a finite-element modelling tool, it is very advanced and can be used to model problems in electromagnetics, structural mechanics, chemical engineering, acoustics and many other fields. A solution to an early test geometry is given in figure 3-1, where surface charge density is plotted on the geometry's surfaces.

As Figure 3-2 shows, the base geometry is first constructed in the GUI-based FEMLAB. The "linear static electrostatic" modelling environment in the electromagnetics module is used with Lagrange (quadratic) elements. Boundary conditions, mesh parameters and a suitable solver are chosen that suit the problem. Boundary conditions that one wishes to set via a script are set as variables. Following this,

50
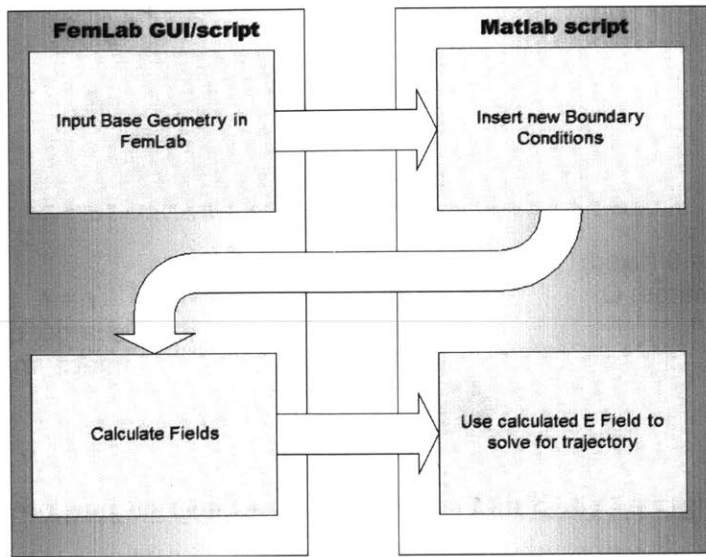
Figure 3-2: Simulation flow for determining cluster trajectory

one can output a MATLAB-style script file which contains code that generates the data structures that represent the geometry, mesh, and other FEMLAB specific directives. The output script is used in conjunction with custom-written MATLAB code that sets many different boundary conditions for a given geometry, and runs particle tracing simulations.

The MATLAB code was written to include many features. Either Euler's method and Runge-Kutta can be used to solve the differential equation given in (3.6). Movies can be generated that plot the geometry and overlay moving particles. Multiple particles trajectories can be simulated simultaneously, as the query to the FEMLAB data structure can be performed for many points. Each particle in multiple particle simulations can have a unique starting position, velocity, charge and mass.

3.3 Verification of Computer Simulation

In order to verify the design flow, a simple geometry was simulated, shown in Figure 3-3. In this test case, a positive charge is held at the origin, while a mobile charge initially at position $\vec{r}_i$ with mass m_o, is imparted with an initial velocity $\vec{v}_i$. The

51
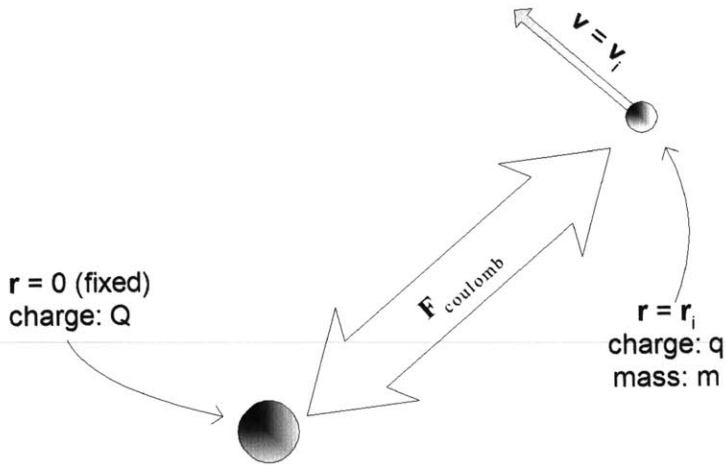
Figure 3-3: Simple case used for verification purposes

advantage of choosing such a geometry is that the equation for the trajectory, which is elliptical, can be found analytically.

3.3.1 Analytical Derivation of Trajectory

To derive a closed form for the trajectory of a particle with charge q, mass m in the presence of a fixed point charge with charge Q, we will use spherical coordinates and give the mobile particle an initial position and velocity in the x-y plane, i.e. where the polar angle θ is $\pi/2$.

We start with Newton's second law as given in (3.1) and expand it in spherical coordinates:

$$
\begin{aligned}
\vec{F} &= m\frac{d^2\vec{r}}{dt^2} \\
&= m\frac{d}{dt}(\dot{r}\,\hat{r} + r\dot{\phi}\,\hat{\phi}) \\
&= m(\ddot{r} - r\dot{\phi}^2)\,\hat{r} + (2\dot{r}\dot{\phi} + r\ddot{\phi})\,\hat{\phi}
\end{aligned} \tag{3.7}
$$

where $\hat{r}$ and $\hat{\phi}$ are the unit vectors pointing in the radial and azimuthal direction

52

respectively, and we have used:

$$\dot{\hat{r}} = \dot{\theta}\,\hat{\theta} \tag{3.8a}$$

$$\dot{\hat{\theta}} = -\dot{\theta}\,\hat{r} \tag{3.8b}$$

Now we define the potential V at radius r due to charge Q at the origin in free space:

$$V = \frac{Q}{4\pi\epsilon_o r} \tag{3.9}$$

The electric field is simply the gradient of the potential:

$$\vec{E} = -\nabla V = \frac{Q}{4\pi\epsilon_o r^2}\,\hat{r} \tag{3.10}$$

The force exerted on a mobile particle with charge q is the well known Coulomb's Law:

$$\vec{F} = q\vec{E} = \frac{qQ}{4\pi\epsilon_o r^2}\,\hat{r} \tag{3.11}$$

Equating (3.11) with (3.7), we find that the $\hat{\phi}$ coefficient is zero, which yields the following equality:

$$
\begin{aligned}
2\dot{r}\dot{\phi} + r\ddot{\phi} &= 0 \\
\frac{2r\dot{r}\dot{\phi} + r^2\ddot{\phi}}{r} &= 0 \\
\frac{1}{r}\frac{d}{dt}(r^2\dot{\phi}) &= 0 \\
\Rightarrow \quad r^2\dot{\phi} &= h
\end{aligned}
\tag{3.12}
$$

where h is a constant for all time.

Now we equate the $\hat{r}$ coefficients:

$$
\begin{aligned}
m(\ddot{r} - r\dot{\phi}^2) &= \frac{qQ}{4\pi\epsilon_o r^2} \\
\ddot{r} - r\dot{\phi}^2 &= \left(\frac{qQ}{4\pi\epsilon_o m}\right)\frac{1}{r^2}
\end{aligned}
\tag{3.13}
$$

Here we define

$$\alpha \equiv \frac{qQ}{4\pi\epsilon_o m} \tag{3.14}$$

Substituting into (3.13), we get

$$
\begin{aligned}
2\dot{r}\ddot{r} - 2\dot{r}r\dot{\phi}^2 &= \frac{2\alpha\dot{r}}{r^2} \\
2\dot{r}\ddot{r} - \frac{2\dot{r}h^2}{r^3} &= \frac{2\alpha\dot{r}}{r^2} \\
\frac{d}{dt}\left(\dot{r}^2 + \frac{h^2}{r^2} + 2\alpha r\right) &= 0 \\
\Rightarrow \quad \dot{r}^2 + \frac{h^2}{r^2} + 2\alpha r &= C
\end{aligned}
\tag{3.15}
$$

Equation (3.15) is a differential equation which is only in r and contains only one time derivative. However, it is easier to solve for the trajectory by removing the time dependence via the following substitution:

$$
\begin{aligned}
u &\equiv \frac{1}{r} \tag{3.16} \\
\frac{du}{dr} &= -\frac{1}{r^2} = -u^2 \\
\dot{r} &= \frac{dr}{du}\frac{du}{d\phi}\frac{d\phi}{dt} \\
&= -\frac{1}{u^2}\frac{du}{d\phi}\dot{\phi} \\
\dot{r} &= -h\frac{du}{d\phi} \\
\Rightarrow \quad \dot{r}^2 &= h^2\left(\frac{du}{d\phi}\right)^2 \tag{3.17}
\end{aligned}
$$

Substitution of (3.16) and (3.17) into (3.15) gives

$$h^2\left(\frac{du}{d\phi}\right)^2 + h^2 u^2 + 2\alpha u = C$$

which is differentiated with respect to ϕ to give

$$2h^2 \frac{du}{d\phi} \frac{d^2u}{d\phi^2} + 2h^2 u \frac{du}{d\phi} + 2\alpha \frac{du}{d\phi} = 0$$

$$h^2 \frac{d^2u}{d\phi^2} + h^2 u + \alpha = 0$$

$$\Rightarrow \quad \frac{d^2u}{d\phi^2} + u = -\frac{\alpha}{h^2} \tag{3.18}$$

Equation (3.18) has the general solution

$$u(\phi) = -\frac{\alpha}{h^2} + c_1 \cos\phi + c_2 \sin\phi \tag{3.19}$$

which can be rewritten by using (3.16) as

$$\boxed{r(\phi) = \frac{1}{c_1 \cos\phi + c_2 \sin\phi - \alpha/h^2}} \tag{3.20}$$

Equation (3.20), when plotted on a polar plot, is the equation for an ellipse, as expected.

To solve for c_1 and c_2, we use knowledge of r_i and ϕ_i, namely that we know initial position of the particle, and also $\dot{r}_i$ and $\dot{\phi}_i$, since we know the initial velocity of the particle. Inserting this into (3.20) and its derivative, we will solve the following system of equations:

$$r_i = \frac{1}{c_1 \cos\phi_i + c_2 \sin\phi_i - \alpha/h^2}$$

$$\dot{r}_i = h(c_1 \sin\phi_i - c_2 \cos\phi_i)$$

which yields

$$c_1 = \frac{\dot{r}_i r_i^2 \dot{\phi}_i \sin\phi_i + (\alpha + r_i^3 \dot{\phi}_i^2) \cos\phi_i}{r_i^4 \dot{\phi}_i^2} \tag{3.21a}$$

$$c_2 = \frac{-\dot{r}_i r_i^2 \dot{\phi}_i \cos\phi_i + (\alpha + r_i^3 \dot{\phi}_i^2) \sin\phi_i}{r_i^4 \dot{\phi}_i^2} \tag{3.21b}$$

We can further relate r_i, ϕ_i, $\dot{r}_i$ and $\dot{\phi}_i$ to their cartesian equivalents via

$$x_i = r_i \cos\phi_i \tag{3.22a}$$

$$y_i = r_i \sin\phi_i \tag{3.22b}$$

$$\dot{x}_i = \dot{r}_i \cos\phi_i - r_i\dot{\phi}_i \sin\phi_i \tag{3.22c}$$

$$\dot{y}_i = \dot{r}_i \sin\phi_i + r_i\dot{\phi}_i \cos\phi_i \tag{3.22d}$$

We will use (3.20) with (3.21) and (3.22) in the following simulation to verify the code and flow.

3.3.2 Computer Simulation

Although the trajectory was simple to derive for this test case, a FEMLAB based simulation involved some advanced finite-element modelling techniques in setting boundary conditions.

The first problem is how to implement a point charge in finite element modelling. FEMLAB provides for setting "weak" boundary conditions for such implementations. In addition, an adaptive solver was used which increases the number of mesh volume elements as one approaches the singularity. The mesh is shown in Figure 3-4 for this geometry.

Another problem is implementing the boundary condition of a vanishing field as $r \to \infty$. This problem was solved by using a spherical enclosure for the point charge. From symmetry, we know the sphere is an equipotential surface, so it is simple to set a boundary condition derived from (3.9).

The field was calculated for the initial conditions given in Table 3.1, and is plotted in Figure 3-5(a). As one can see from this plot and from the adjoining plot in Figure 3-5(b), the model is correct to within 1% after r=0.5m. The initial conditions for position and velocity were chosen to minimize error from the model, however it is important to note this additional source of error.

The trajectory the particle takes is shown in Figure 3-6. Upon close inspection,
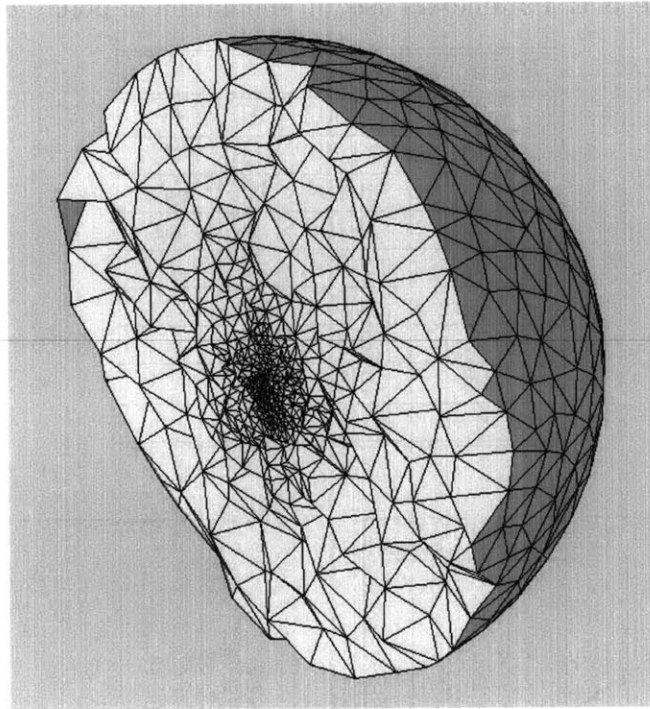
Figure 3-4: Mesh generated for geometry with point charge at origin

one can see that the trajectory traversed by the solution obtained by Euler's method is less accurate than that obtained via the Runge-Kutta method. However, the trajectory obtained via the Runge-Kutta method is closer to the theoretical path, with cumulative errors in position and velocity, coupled with a large time step and errors in the field contributing to the total error after one revolution. However, the proximity of the solution verifies that the MATLAB code is working correctly. Now the code can be subjected to the geometry of interest in this thesis.

3.4   Simulation of Cluster Flight

A suitable geometry that will exemplify the approach of cluster rejection while attracting a majority of clusters for certain initial conditions is sought. The following section walks through the boundary conditions, both static and variable, and the field solution for the chosen geometry.

Table 3.1: Parameters used in simulation of point charge

Parameter	Value
q	1.602×10^{-19} C
Q	-1.602×10^{-19} C
ϵ_o	8.854×10^{-12} F/m
m	9.109×10^{-31} kg
r_i	2.9 m
ϕ_i	$\pi/5$ rad
$\dot{r}_i$	0.3 m/s
$\dot{\phi}_i$	2.3 rad/s
time step	10 ms

(a) Potential due to a point charge   (b) Error in calculation
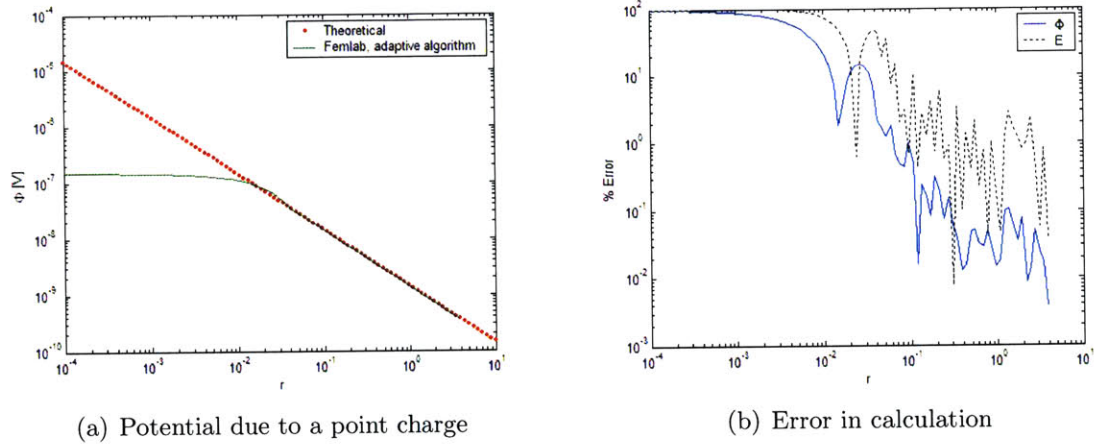
Figure 3-5: FEMLAB field calculations of point charge located at the origin

3.4.1 Field Calculations

The geometry that was simulated is shown in Figure 3-7(a). As was the issue in the previous problem, the boundary conditions in a finite-element geometry should be defined on the drawn geometry[1]. Given the scale of the problem, the nearest ground plane to the substrate is the sample holder (or aluminium stub), which is usually grounded, hence is where the field lines terminate. Two potentials are applied: a positive potential V_{in}, to a circle of radius 0.1μm, and V_{out}, a negative potential to the annulus with outer radius 1μm that surrounds the circle. This is shown in Figure 3-7(b).

---

[1]That is, vanishing boundary conditions like $\Phi \to 0$ at $r \to \infty$ cannot be defined.
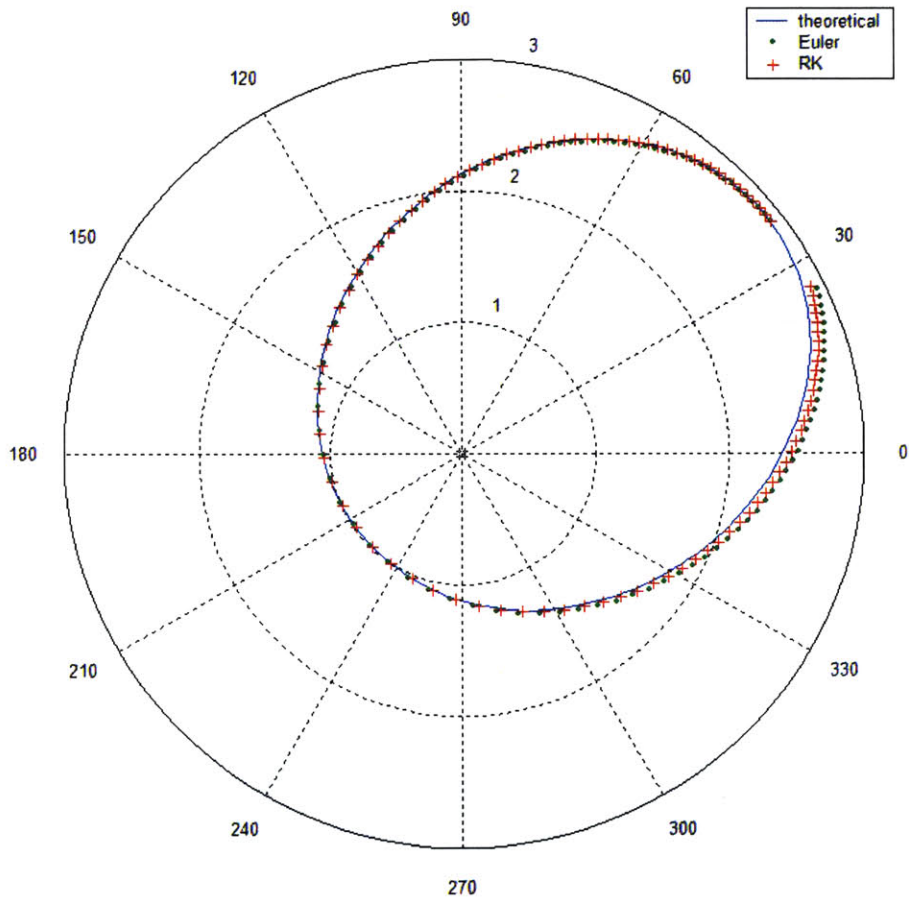
Figure 3-6: Trajectory of a particle in the field due to a point charge located at the origin

All other boundaries are *insulating*, meaning that field lines are continuous through the boundary. The substrate was given a relative permittivity (ϵ_r) of 4, similar to that of insulators like glass. After the boundary conditions were applied, a fine mesh was generated. A cross-section is shown in Figure 3-8. This cross-section shows the increase in mesh elements as one approaches the center of the substrate, where the potentials are applied.

The simulation is then run for many different values of V_{in} and V_{out}. The values used for V_{in} were 150, 100, 90, 80, 70, 60, 50, 40, 30, 20, 10, 8, 5, 2, 1 and 0V, while those for V_{out} were -40, -30, -20, -10, -5, -1, -0.1, -0.05, -0.01 and 0V . Each combination of values was applied as boundary conditions to the geometry, creating

(a) Full view

(b) Close-up view, showing potentials applied in simulated geometry
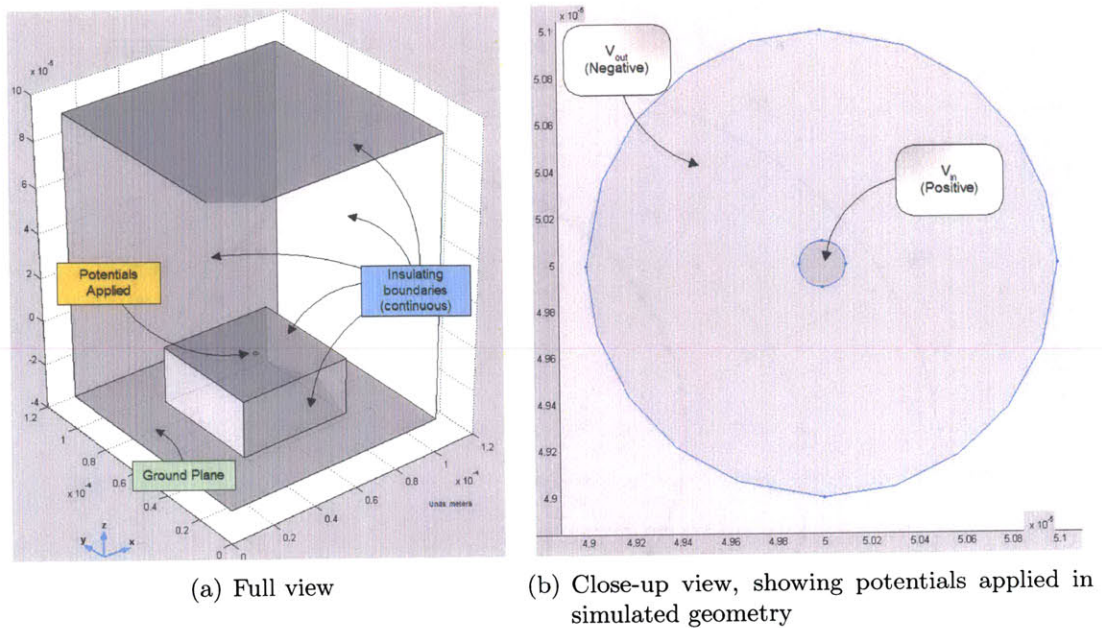
Figure 3-7: Simulated Geometry
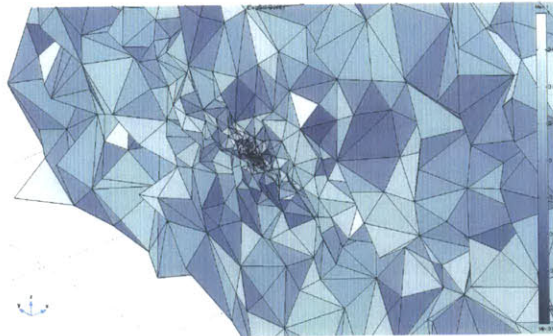
Figure 3-8: Cross-section of mesh for simulated geometry

160 trials in all. A typical surface density plot of the substrate region near the potentials is shown in Figure 3-9.

3.4.2 Initial Conditions

The Runge-Kutta simulation was carried out with the initial conditions given in Table 3.2. The cluster mass corresponds to the mass of 50 copper atoms, while the charge to the electronic charge of one electron.

The initial position of the particles was not randomized for this simulation. The

60

Figure 3-9: Surface charge density around region of interest

Table 3.2: Simulation conditions

Cluster mass	5.278e-24 kg
Charge	-1.602×10^{-19} C
Average kinetic energy	2.5eV
Energy spread	25meV
Average velocity	389m/s
Standard deviation of velocity	19.47m/s
Number of clusters/trial	80
Initial height (z)	10um
Step size	0.1ns

spatial distribution that was used is given in Figure 3-10(a). The velocity distribution, however, was randomized using a normal distribution centered around the average velocity as given in Table 3.2. The typical velocity distribution for a trial is given in Figure 3-10(b). The particles were traced via solving the differential equation (3.6) for each field solution using the Runge-Kutta method.

3.5 Simulation Results

The data produced from this simulation was very large, but a compact form is presented in Figure 3-11. Figure 3-11(a) and 3-11(b) show the values that were used for V_{in} and V_{out} (given on the x-axis) for each trial (trial # given on the y-axis of each plot). Figure 3-11(c) shows the results in a topographical image. The color of each pixel represents the percentage of clusters that land in a 50nm wide bin, while the distance of each pixel in the lateral direction represents the radial distance of each
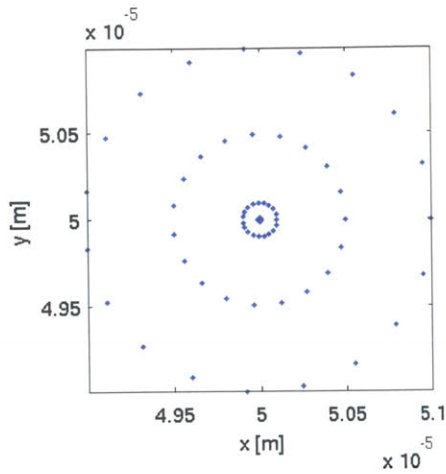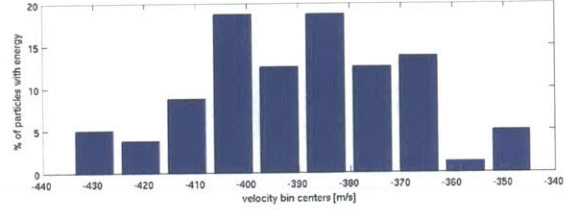
(a) Spatial distribution   (b) Typical velocity distribution

Figure 3-10: Spatial and velocity distribution of clusters

bin from the origin. The last column of pixels in the image represents the clusters that get rejected by the repulsive potentials on the substrate.

Figure 3-11 shows that in a large number of trials (1-63), the incoming clusters were totally rejected by the repulsive potential. The potentials applied in trials 75 and beyond appear not to be able to reject clusters, with a large proportion of clusters landing away from the desired target. Trials 64-74 are of interest, as there appears to be a high degree localization near the origin of incoming clusters and a high degree of rejection. These trials are replotted in the Figure 3-12 so that the optimal applied potential can be identified.

From close examination of Figure 3-12, it appears that the potentials of $V_{in} = 60V$ and V_{out}=-5V give the best results (47.5% hit the target while 27.5% are rejected). This trial is compared to one where there is no repulsive potential applied (V_{out}=0V). Figure 3-13 illustrates the subtlety of the difference in field due to the negative potential, whereas the power of the repulsive force is illustrated in Figure 3-14. Figure 3-15 shows the actual trajectories taken by clusters in this simulation. Note that the z=0 plane is that of the substrate.
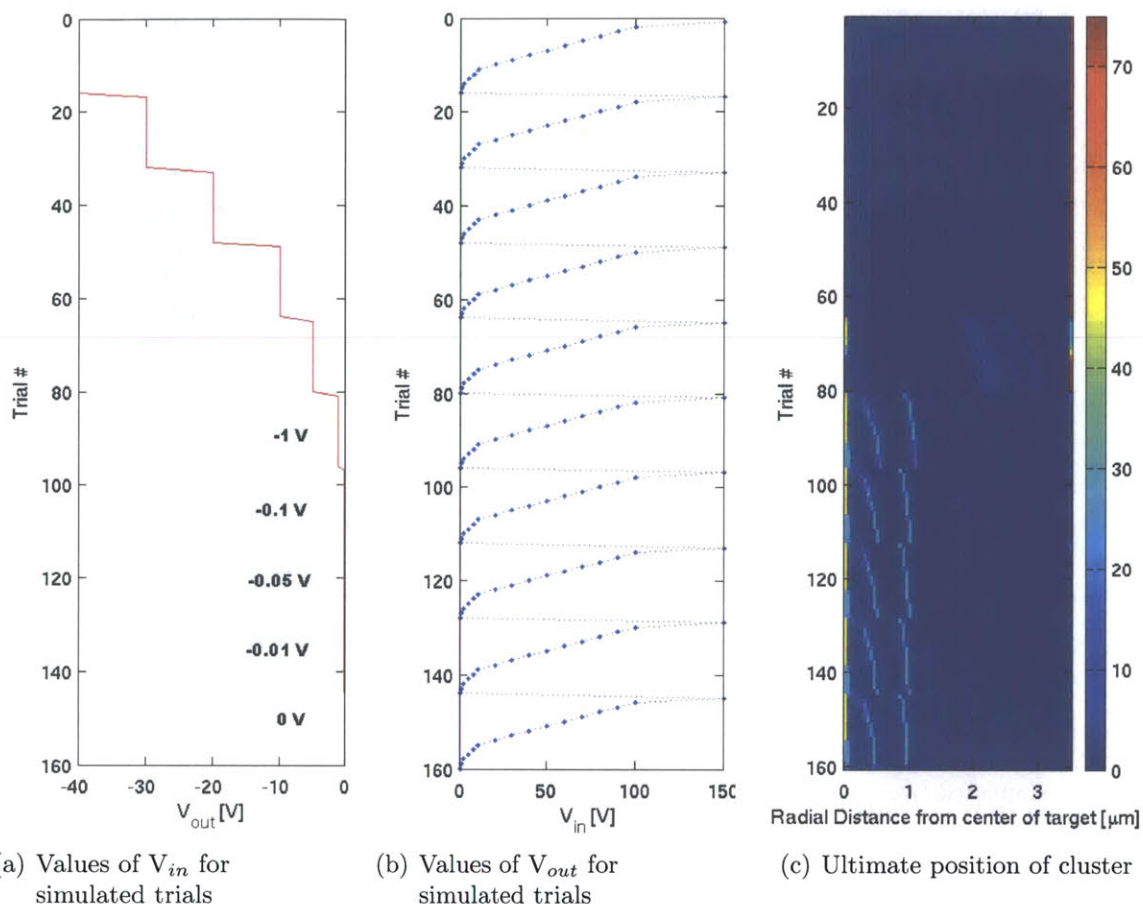
(a) Values of V_{in} for simulated trials

(b) Values of V_{out} for simulated trials

(c) Ultimate position of cluster

Figure 3-11: Simulation results for all trials. Pixels in (c) are color-coded by the percentage of clusters that fall in the 50nm bin. Note that the right-most column in (c) color-codes clusters that do not impact the surface.

3.6 Future Work

Although many of the parameters in this simulation were contrived, this example illustrates that the framework exists to make this calculation useful in predicting particle trajectory, once accurate parameters are discovered about the clusters generated in our system. From the geometry that was simulated, one can conclude that (for the given initial conditions) there is an optimal set of potentials that can guide a sizable proportion of incoming clusters to a localized circular area of radius 100nm, while rejecting wayward particles. This simulation also shows that the approach of using both positive and negative potentials to define an electrostatic lens or filter, in the context of *nanoxerography*, shows promise in improving pattern definition and

(a) Values of V_{in} for simulated trials

(b) Values of V_{out} for simulated trials

(c) Ultimate position of cluster
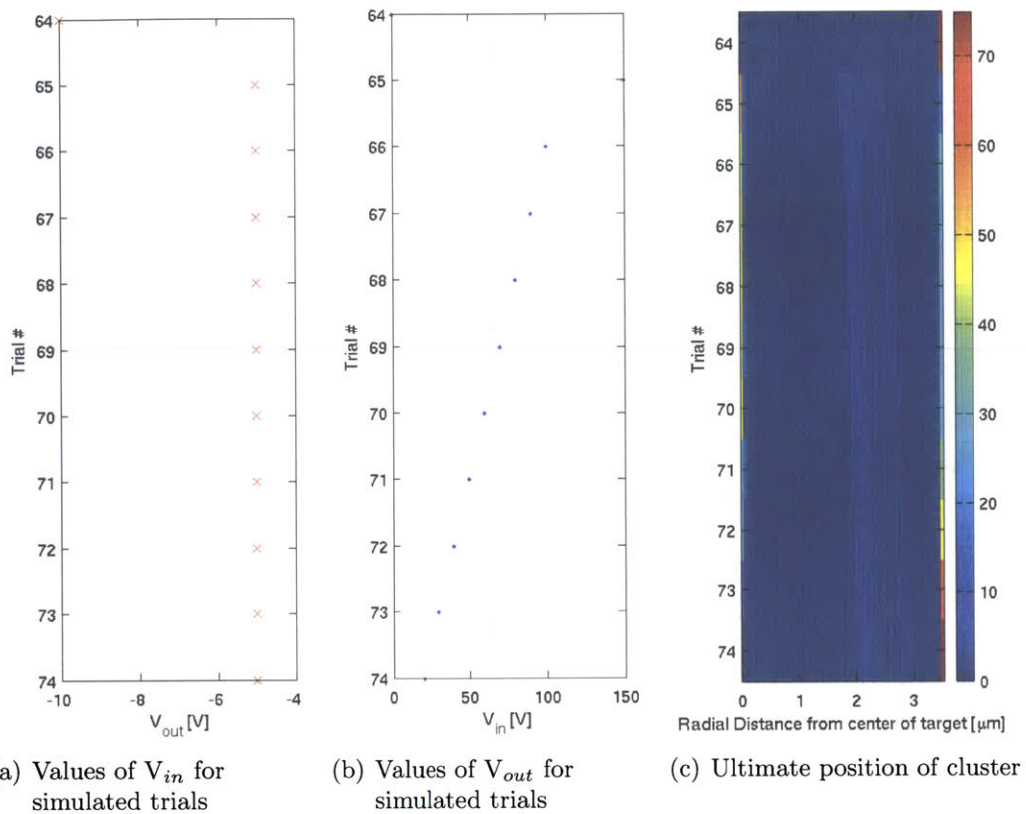
Figure 3-12: Simulation results for trials 65 - 74. Note that the right-most column in (c) color-codes clusters that do not impact the surface

fidelity. Future simulation work can tackle the problem of accurately guiding particle trajectories to more complicated charge geometries, such as the layout of a circuit. Additionally, if the clusters are decelerated by apparatus before being subjected to the potentials on the substrate, one would need to take the forces that were neglected in this calculation, such as the stochastic force and van der Waals force, into account.

(a) V_{in}=60V, V_{out}=0V
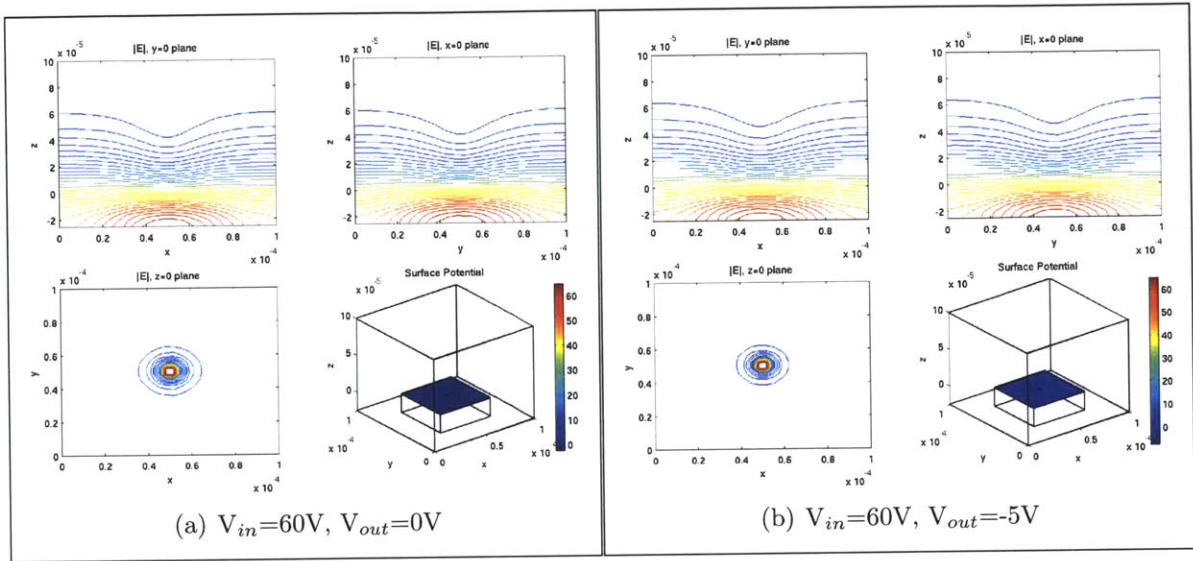
(b) V_{in}=60V, V_{out}=-5V

Figure 3-13: Electric Field for clusters in two trials

(a) V_{in}=60V, V_{out}=0V

(b) V_{in}=60V, V_{out}=-5V

Figure 3-14: Impact position for clusters in two trials
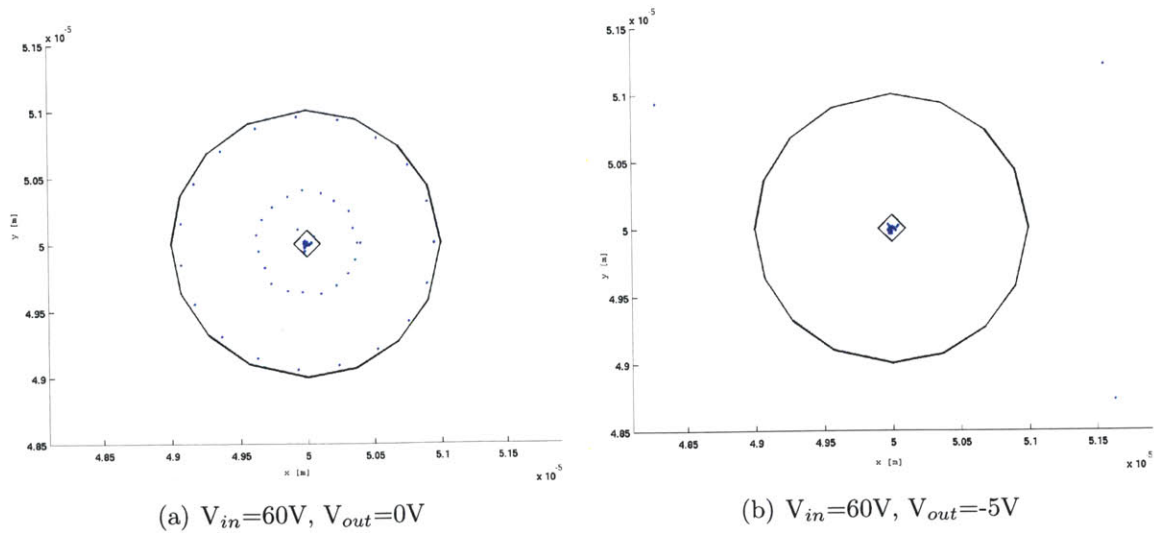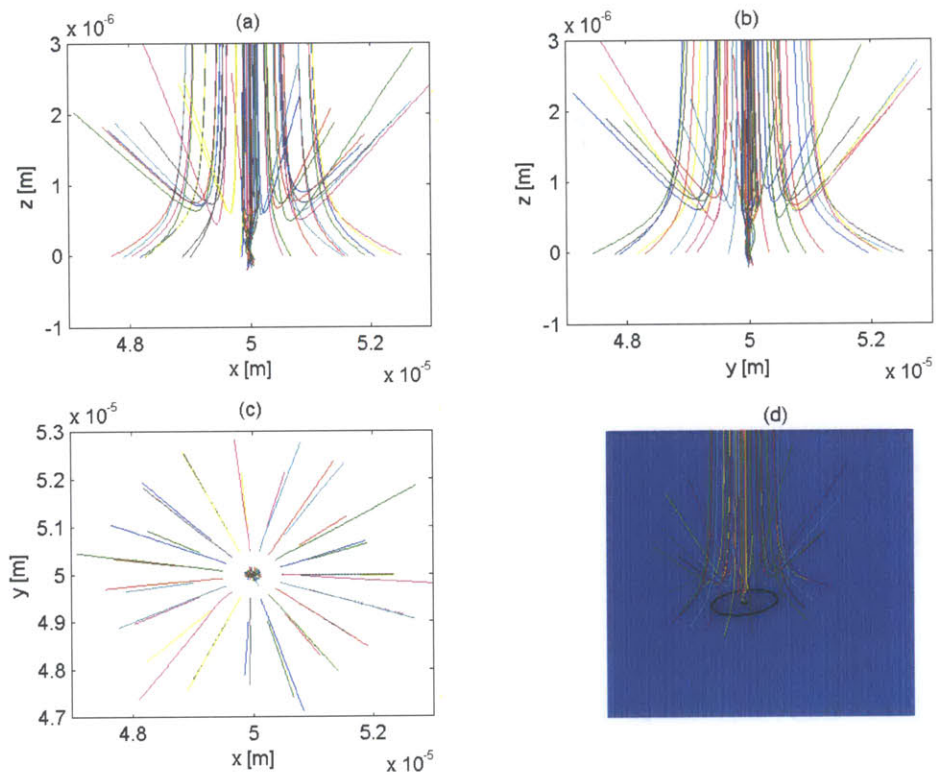
Figure 3-15: Particle trajectories for V_{in}=60V, V_{out}=-5V. (a) y=0 plane, (b) x=0 plane, (c) z=0 plane, (d) perspective view near surface

66

Chapter 4

Concluding Remarks

One of the most important goals of *nanoxerography*, from a research viewpoint, is to enable a user, who may be uninitiated to conventional fabrication, to rapidly prototype complex devices on the nanoscale. If users are able to accurately build prototypes of a device, say a 3D transistor, even if the build time is on the order of days, it can remove the need to master the use of the arcane machinery that generally populates an IC fabrication facility and weeks of processing time.

As the title of this thesis suggests, the work presented in this thesis is a framework that will enable the process of *nanoxerography* to be realized. However, it leaves many issues unaddressed. There are further points of study, other than those mentioned previously in the chapters, that have far-reaching consequences. One very important aspect is designing, from a theoretical foundation, the three-dimensional devices that can be constructed using the *nanoxerography* process. Whether this device will be based on conventional FET devices, whether it will utilize quantum effects or even field-emission principles for gain are questions that need to be addressed. Such a device has to be designed so that it is error-tolerant both in the manufacturing process and in its operational state.

Another very interesting aspect of *nanoxerography* that can be studied is its application to areas other than integrated circuit manufacturing. If the principles of *nanoxerography* can be used to guide charged biological molecules to specific sites on a substrate, then this process has the possibility to revolutionize the biotechnology

industry, as one does not have to rely on stochastic processes to bind molecules to sites. Rather, a strategy similar to those used in dip-pen nanolithography to pattern biological molecules [34,35] can be used, but in this case, the process would be many orders of magnitude faster.

Bibliography

[1] L. Van den hove, A. M. Goethals, K. Ronse, M. Van Bavel, and G. Vandenberghe. Lithography for sub-90nm applications. In *International Electron Devices Meeting*, San Francisco, 2002.

[2] H. O. Jacobs, S. A. Campbell, and M. G. Steward. Approaching nanoxerography: The use of electrostatic forces to position nanoparticles with 100 nm scale resolution. *Advanced Materials*, 14(21):1553, 2002.

[3] H. Haberland, M. Karrais, and M. Mall. A new type of cluster and cluster ion-source. *Z Phys D Atom Mol Cl*, 20(1-4):413–415, 1991.

[4] M. S. Gudiksen, L. J. Lauhon, J. Wang, D. C. Smith, and C. M. Lieber. Growth of nanowire superlattice structures for nanoscale photonics and electronics. *Nature*, 415(6872):617–20, 2002.

[5] L. J. Lauhon, M. S. Gudiksen, D. Wang, and C. M. Lieber. Epitaxial core-shell and core-multishell nanowire heterostructures. *Nature*, 420(6911):57–61, 2002.

[6] Y. Huang, X. Duan, Q. Wei, and C. M. Lieber. Directed assembly of one-dimensional nanostructures into functional networks. *Science*, 291(5504):630–3, 2001.

[7] C. M. Lieber. Nanowire superlattices. *Nano Letters*, 2(2):81–82, 2002.

[8] K. Mukhopadhyay and G. N. Mathur. Bimetallic catalyst for synthesizing quasi-aligned, well-graphitized multiwalled carbon nanotube bundles on a large scale by the catalytic chemical vapor deposition method. *J Nanosci Nanotechnol*, 2(2):197–201, 2002.

[9] J. C. Charlier, A. De Vita, X. Blase, and R. Car. Microscopic growth mechanisms for carbon nanotubes. *Science*, 275(5300):646–9, 1997.

[10] F. Rohmund, R. E. Morjan, G. Ledoux, F. Huisken, and R. Alexandrescu. Carbon nanotube films grown by laser-assisted chemical vapor deposition. *J Vac Sci Technol B*, 20(3):802–811, 2002.

[11] A. Bachtold, P. Hadley, T. Nakanishi, and C. Dekker. Logic circuits with carbon nanotube transistors. *Science*, 294(5545):1317–20, 2001.

[12] Y. Cui and C. M. Lieber. Functional nanoscale electronic devices assembled using silicon nanowire building blocks. *Science*, 291(5505):851–3, 2001.

[13] Y. Zhang, K. Suenaga, C. Colliex, and S. Iijima. Coaxial nanocable: silicon carbide and silicon oxide sheathed with boron nitride and carbon. *Science*, 281(5379):973–5, 1998.

[14] R. J. Jackman, S. T. Brittain, A. Adams, M. G. Prentiss, and G. M. Whitesides. Design and fabrication of topologically complex, three-dimensional microstructures. *Science*, 280(5372):2089–91, 1998.

[15] M. Mutzel, S. Tandler, D. Haubrich, D. Meschede, K. Peithmann, M. Flaspohler, and K. Buse. Atom lithography with a holographic light mask. *Phys Rev Lett*, 88(8):083601, 2002.

[16] L. R. Baylor, D. H. Lowndes, M. L. Simpson, C. E. Thomas, M. A. Guillorn, V. I. Merkulov, J. H. Whealton, E. D. Ellis, D. K. Hensley, and A. V. Melechko. Digital electrostatic electron-beam array lithography. *J. Vac. Sci. Technol. B*, 20(6):2646–2650, 2002.

[17] J. G. Hartley, T. R. Groves, H. I. Smith, M. K. Mondol, J. G. Goodberlet, M. L. Schattenburg, J. Ferrera, and A. Bernshteyn. Spatial-phase locking with shaped-beam lithography. *Review of Scientific Instruments*, 74(3):1377–1379, 2003.

[18] Y. Martin and H. K. Wickramasinghe. Magnetic imaging by force microscopy with 1000-a resolution. *Appl Phys Lett*, 50(20):1455–1457, 1987.

[19] H. O. Jacobs, P. Leuchtmann, O. J. Homan, and A. Stemmer. Resolution and contrast in kelvin probe force microscopy. *Journal of Applied Physics*, 84(3):1168–1173, 1998.

[20] J. M. R. Weaver and D. W. Abraham. High-resolution atomic force microscopy potentiometry. *J Vac Sci Technol B*, 9(3):1559–1561, 1991.

[21] M. Nonnenmacher, M. P. Oboyle, and H. K. Wickramasinghe. Kelvin probe force microscopy. *Appl Phys Lett*, 58(25):2921–2923, 1991.

[22] Y. Martin, D. W. Abraham, and H. K. Wickramasinghe. High-resolution capacitance measurement and potentiometry by force microscopy. *Appl Phys Lett*, 52(13):1103–1105, 1988.

[23] H. O. Jacobs, H. F. Knapp, S. Muller, and A. Stemmer. Surface potential mapping: A qualitative material contrast in SPM. *Ultramicroscopy*, 69(1):39–49, 1997.

[24] M. Kotera, K. Yamaguchi, and H. Suga. Dynamic simulation of electron-beam-induced chargingup of insulators. *Jpn. J. Appl. Phys. Part 1 - Regul. Pap. Short Notes Rev. Pap.*, 38(12B):7176–7179, 1999.

[25] X. K. Qin, K. Suzuki, Y. Tanaka, and T. Takada. Three-dimensional space-charge measurement in a dielectric using the acoustic lens and pwp method. *J. Phys. D-Appl. Phys.*, 32(2):157–160, 1999.

[26] H. Gong, Z. G. Song, and C. K. Ong. Space-charge dynamics of poly-methylmethacrylate under electron beam irradiation. *J. Phys.-Condes. Matter*, 9(23):5027–5031, 1997.

[27] Z. G. Song, H. Gong, and C. K. Ong. The trapping and distribution of charge in polarized polymethylmethacrylate under electron-beam irradiation. *J. Phys. D-Appl. Phys.*, 30(11):1561–1565, 1997.

[28] H. O. Jacobs and G. M. Whitesides. Submicrometer patterning of charge in thin-film electrets. *Science*, 291(5509):1763–1766, 2001.

[29] D M Taylor. The effect of passivation on the observation of voltage contrast in the scanning electron microscope. *Journal of Physics D: Applied Physics*, 11(18):2443, 1978.

[30] W. Liu, J. Ingino, and R. F. Pease. Resist charging in electron beam lithography. *J. Vac. Sci. Technol. B*, 13(5):1979–1983, 1995.

[31] T. J. Krinke, K. Deppert, M. H. Magnusson, F. Schmidt, and H. Fissan. Microscopic aspects of the deposition of nanoparticles from the gas phase. *J Aerosol Sci*, 33(10):1341–1359, 2002.

[32] William C. Hinds. *Aerosol technology : properties, behavior, and measurement of airborne particles.* Wiley, New York, 2nd edition, 1999.

[33] S. R. Coon, W. F. Calaway, M. J. Pellin, and J. M. White. New findings on the sputtering of neutral metal-clusters. *Surf Sci*, 298(1):161–172, 1993.

[34] K. B. Lee, S. J. Park, C. A. Mirkin, J. C. Smith, and M. Mrksich. Protein nanoarrays generated by dip-pen nanolithography. *Science*, 295(5560):1702–5, 2002.

[35] L. M. Demers, D. S. Ginger, S. J. Park, Z. Li, S. W. Chung, and C. A. Mirkin. Direct patterning of modified oligonucleotides on metals and insulators by dip-pen nanolithography. *Science*, 296(5574):1836–8, 2002.

List of Acronyms

AFM atomic force microscopy.

KFM kelvin probe microscopy. A non-contact form of atomic force microscopy (AFM) where an ac-bias is applied to the tip, whose phase is tracked and nulled via a dc bias when influenced by sample-induced forces, such as force due to surface charge.

kV kiloVolt. A unit of potential equal to a thousand volts.

CAD computer-aided design.

CVD chemical vapor deposition.

EFM electrostatic force microscopy. A non-contact form of atomic force microscopy (AFM) where a potential is applied to the tip as it is scanned on a sample.

ESEM environmental scanning electron microscope. A microscope that allows for electron imaging of non-conducting samples via the use of an imaging gas, such as water vapor, and special detectors.

FIB focussed ion beam (microscope). Generally used when referring to a microscope that uses a focussed beam of ions to image, mill or deposit material.

HV high vacuum. As a rough guideline, a system is considered to be in high vacuum (HV) if the pressure is between 10^{-6} to 10^{-8} Torr.

ITRS International Technology Roadmap for Semiconductors. For more information, visit http://public.itrs.net/

MEMS Micro-Electro-Mechanical Systems.

NPGS Nanometer Pattern Generation System. A commercial software package used with the ESEM to enable lithography applications.

PMMA poly(methylmethacrylate).

PET polyethylene terepthalate.

PTFE polytetrafluoroethylene.

SEM scanning electron microscope.

TEM transmission electron microscopy.

UHV ultra high vacuum. As a rough guideline, a system is considered to be in ultra high vacuum (UHV) if the pressure is below 10^{-9} Torr.